공학석사 학위논문

An investigation on Cu-based amorphous binary alloy for efficient reduction of CO_2 into useful fuels

효율적으로 이산화탄소를 연료로 환원하기 위한 구리 기반 비정질 이원계 합금에 대한 연구

2017 년 2 월

서울대학교 대학원

재료공학부

이 준 호

Abstract

An investigation on Cu-based amorphous binary alloy for efficient reduction of CO_2 into useful fuels

Jun Ho Lee

Department of Materials Science and Engineering

The Graduate School

Seoul National University

Electrocatalytic conversion of CO_2 to useful fuels has potential advantages as a method to use CO_2 as a chemical feedstock in terms of using water as a proton source at ambient condition and being easily combined with renewable energy. Thus far, electrochemical conversion of CO_2 into useful fuels (formate, carbon monoxide, methanol and so on) has been successfully demonstrated, however, the production of C_4 or longer hydrocarbons as a major product has never been achieved. Thus, our group focused on developing a new

platform of catalysts which could lead to efficient production of long chain hydrocarbons beyond currently available C_1, C_2 and C_3 chemicals.

In this research, we adopted amorphous Cu–Ti as new CO_2 reduction electrode to enhance activity for the synthesis of long chain hydrocarbons. At first, to understand the effect of atomic concentration, CO_2 reduction reaction (CO_2RR) properties of amorphous Cu–Ti alloys with different compositions ($Cu_{40}Ti_{60}$, $Cu_{50}Ti_{50}$, $Cu_{60}Ti_{40}$) were evaluated using cyclic voltammetry (CV). Amorphous $Cu_{40}Ti_{60}$ exhibited the best catalytic performance and required the least overpotential to reach partial current density of 1 mA cm^{-2} for CO_2 reduction. The outstanding property was explained by stronger binding affinity of the electrode to carbon oxygenates, as shown by CO_2–TPD. These observations indicate that Ti is responsible for increasing the bond strength between electrode surface and reaction intermediates.

Next, we found that amorphous $Cu_{40}Ti_{60}$ electrode has superior catalytic activity for butanol formation. Product analysis after bulk electrolysis by gas chromatography (GC) and nuclear magnetic

resonance (NMR) confirmed the production of n-butanol, acetaldehyde, methyl formate, CO, H_2 and so on. This was the first to report C_4 product (n-butanol) with high Faradaic efficiency (25%) from the reduction of CO_2. This result implies that amorphous nature of alloy induced strong interaction with carbon oxygenates and facilitated C-C bond formation of adsorbate. Moreover, potential dependent product analysis was conducted in order to construct the reaction mechanism from CO_2 to n-butanol. As a result, it was suggested that butanol was produced by condensation of two C_2 intermediates, excluding possibility of chain addition to create C_3 intermediate.

In this study, we successfully produced C_4 products from CO_2RR by using amorphous $Cu_{40}Ti_{60}$ alloy as a working electrode. From this result, we could provide valuable insights for developing efficient CO_2 conversion pathway for long chain hydrocarbons using C_2 building blocks. It was achieved by introducing amorphous binary alloys which were capable of controlling atomic composition and its arrangement.

Keywords: Carbon dioxide reduction, electrocatalyst, amorphous alloy

Student Number: 2015-20858

Contents

List of Tables

List of Figures

Chapter 1. Introduction

1.1 Global warming and atmospheric CO_2 level

Global warming is currently one of the most well-known environment concern throughout the world. Since industrial revolution, the global temperature has increased significantly. The global temperature rise can be observed clearly even after 1950s[1]. As shown in Figure 1.1 a), land surface air temperature has increased about 1.2 ℃ in last 60 years, thus making average global temperature of the recent years the highest on record[2]. The consequence of this temperature increase can be easily discovered from the environment. Glaciers are rapidly melting and sea levels are rising by more than 0.2 cm/yr[1]. The temperature rise within projections of the Intergovernmental Panel on Climate Change (IPCC) forecasting models[3]. These models correlate global warming with atmospheric CO_2 level.

These days, a strong relationship between global temperature and atmospheric CO_2 level is a widely accepted explanation of global warming. Since industrial revolution, atmospheric level of CO_2, a greenhouse gas (GHG), has increased due to usage of fossil fuels,

deforestation and human activities. Atmospheric CO_2 concentration has increased by almost 100 ppm since industrial revolution, exceeding 400 ppm for the first time in 2015 (Figure 1.1 b))[4]. This gradual increase of CO_2 level in the atmosphere is known to be responsible for global temperature because greenhouse gas to escape the earth's atmosphere.

Many people including politicians and scientists are aware of this situation and the risks which can be caused by irreversible consequences of human-induced global warming[5]. Concerns on global warming have led to concerted actions that mainly focus on preventing further temperature rise and limiting GHG (CO_2) emission. One of the most recently taken global action is the twenty-first Conference of the Parties (COP21), which took place in Paris in December 2015. In COP21, countries were asked to publicly declare what actions they intend to take under a new global agreement which aims to reduce global GHG emissions to restrict global temperature rise to 2 ° C. As a result of the COP21 talks, called the Paris agreement, South Korea needs to mitigate its GHG emission by 37% until 2020. Therefore, researches on technologies to mitigate atmospheric CO_2 must be conducted.

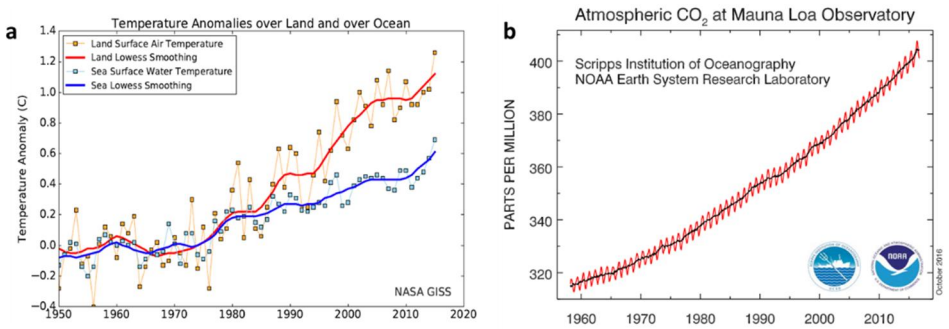

Figure 1.1 a) Temperature anomalies over land and over ocean after 1950, and b) increase of atmospheric CO_2 level at Manua Loa Observatory

1.2 Carbon capturing technologies

In order to mitigate CO_2 emission, many scientists have investigated on technologies to capture CO_2 in the atmosphere. Two commonly used technologies are carbon capture and sequestration (CCS) and carbon capture and utilization (CCU)[6,7].

CCS is a technique which captures waste carbon dioxide by adsorption or membrane gas separation technologies and deposits it normally into underground geological formation (Figure 1.2). Typically, captured gas is stored in depleted gas fields or oil fields which are located few kilometers deep from the crust of the Earth. Over a long time, deposited CO_2 can eventually transform into fuels again under pressure and heat. This can lead to cyclic reproduction of fuels and completion of carbon cycle. However, the long-term storage of CO_2 is a relatively new concept and there are some serious concerns involving safety issues, leakage and the sustainability of the process. In addition, this technique is not suitable in Korea because there are not sufficient amount of depleted oil or gas fields for it.

CCU, on the other hand, is another carbon capturing method in which carbon dioxide is chemically fixed. In CCU, carbon dioxide is

converted into other useful and value-added chemicals by chemical reactions. Therefore, this method can complete nature's carbon cycle, which has been broken since the industrial revolution. Additionally, CCU can provide some insights to use greenhouse gas as a chemical feedstock. Among many methods used in chemical carbon fixation, we mainly focused on electrochemical conversion because it has potential advantages in terms of using water as a proton source, producing value-added chemicals at ambient conditions and, most of all, being easily combined with renewable energy (Figure 1.3)[8].

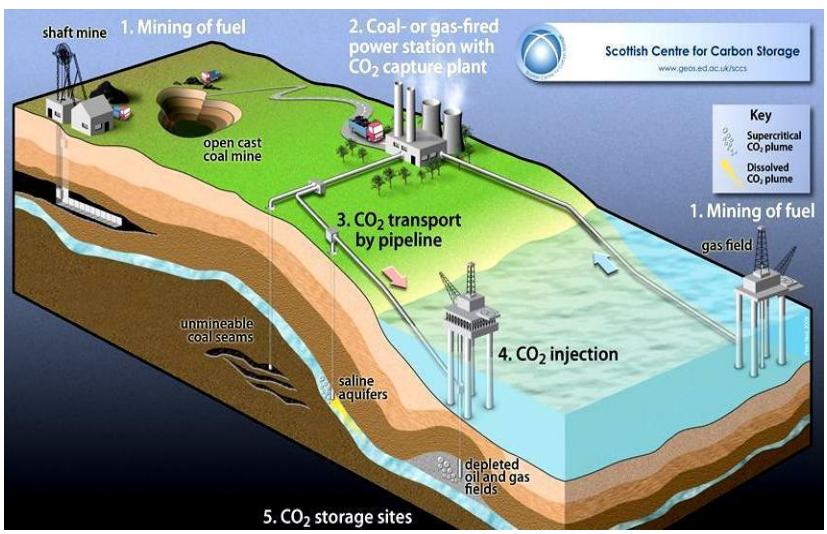

Figure 1.2 A scheme of carbon capture and sequestration (CCS) [9]

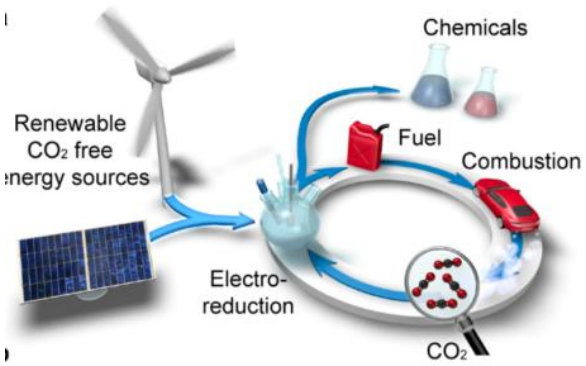

Figure 1.3 General scheme of artificial carbon cycle including electrochemical reduction of CO_2

1.3 Electrochemical reduction of CO_2

1.3.1 Principle of electrochemical reduction of CO_2

Electrochemical reduction of CO_2 is one method to convert carbon dioxide into other useful chemicals. As mentioned above, electrochemical reduction has great advantages over other CO_2 conversion methods ; 1) it can be powered by renewable energy, 2) it has systems which are easy to scale up, 3) the whole process is environmental friendly and 4) the reaction can be conducted in room temperature. Despite its advantages, this method contains several drawbacks including slow kinetics, low catalytic activity and low selectivity.

Electrochemical reduction of CO_2 can proceed through various reduction pathways in aqueous environment at both low and high temperatures[10,11]. The major reduction products are formic acid ($HCOOH$)[12], carbon monoxide (CO)[13,14], methanol (CH_3OH)[15,16], ethylene (C_2H_4)[17,18], propanol (C_3H_7OH)[19] and etc. Thermodynamic standard potentials of half-reactions of CO_2 reduction are shown in Table 1.1[11]. Low selectivity of products mainly contribute to close thermodynamic standard potentials between them. Since all

reduction reactions occur simultaneously, each reaction is a competitive reaction to each other including hydrogen evolution reaction (HER). In addition, high overpotential required to initiate CO_2 reduction results in low catalytic activity and higher activity for HER.

Reaction on cathode	Thermodynamic standard potential (V vs RHE)
$2H^+ + 2e^- \rightleftharpoons H_2$	0.00
$CO_2 + 2H^+ + 2e^- \rightleftharpoons CO + H_2O$	- 0.11
$CO_2 + 6H^+ + 6e^- \rightleftharpoons CH_3OH + H_2O$	+ 0.02
$CO_2 + 8H^+ + 8e^- \rightleftharpoons CH_4 + 2H_2O$	+ 0.16
$2CO_2 + 12H^+ + 12e^- \rightleftharpoons C_2H_4 + 4H_2O$	+ 0.07
$2CO_2 + 12H^+ + 12e^- \rightleftharpoons C_2H_5OH + 3H_2O$	+ 0.08

Table 1.1 Reactions occurring on cathode during electrochemical reduction of CO_2 and there thermodynamic standard potentials.

1.3.2 Previously investigated metal catalysts

To overcome these obstacles, some metals were investigated as electrocatalysts for CO_2 reduction. Investigated metals and their products are given in Table 1.2[11]. According to chemicals they produce, these metals could be divided into four groups – CO group (Au, Ag, Zn, Pd, Ga), HCOOH group (Pb, Hg, Tl, In, Sn, Cd, Bi), H_2 group (Ni, Fe, Pt, Ti) and Cu. The majority of metals are capable of synthesizing only C_1 chemicals (CO, HCOOH). However, Cu electrode can reduce carbon dioxide into various hydrocarbons such as methane, ethylene, ethane and propanol[8]. This extraordinary hydrocarbon conversion rate of Cu makes it a special metal as an electrocatalyst.

The unique characteristic of copper can be explained by simulation results. According to theoretical calculations, Cu has moderate CO binding affinity (Figure 1.4)[20]. Its binding affinity to $CO_{(solv)}$ is weaker than those of metals in HCOOH group and H_2 group, and stronger than those of metals in CO group. This calculation can provide a clue for product trend of metals. Metals with high strong CO binding affinity are likely to be poisoned by CO and further reduction require high activation energies to break the bond. Therefore, they tend to produce more formate than CO, which

requires less overpotential to be synthesized. It is the opposite for metals with weak CO binding affinity. CO, produced by reduction of CO_2, are less likely to stay on the surface of these metals for further reduction. Therefore, they are only capable of producing CO. Since copper has moderate CO binding character, it has ability to adsorb CO and other reaction intermediates during reduction on its surface.

Many researches have focused on altering CO binding energy by changing surface morphology or facets[21–24]. The change in CO binding energy on the electrode surface can affect reaction pathway because it can also affect binding affinity towards reaction intermediates. Table 1.3 shows facet dependence of CO adsorption on Cu electrode[25]. Therefore, controlling facets on the surface can lead to variation in CO_2 reduction pathway[26]. In addition, increase of surface area also increases number of active sites. Consequently, electrodes with large surface area may be capable of producing more chemicals. There are some examples of hydrocarbons which were selectively produced from electrodes based on Cu. First, high methanol yield was achieved using electrodeposited cuprous oxide electrodes[27]. In this work, authors claimed that the yield follows Cu(I) concentration because it can enable hydrogenation of oxygen atoms. Also, high selectivity for ethylene was reported using

nanocube-covered copper[28] electrode. By fabricating Cu nanocube electrodes, a lot of Cu (100) sites were formed. After product analysis, this group found that Cu (100) site, which is known to favor ethylene formation, indeed has the highest selectivity for ethylene at lower overpotential among investigated crystalline surfaces. Lastly, the formation of propanol was observed from chloride induced biphasic Cu_2O-Cu catalyst[19]. This catalyst was reported to have stronger binding affinity towards CO when compared to other biphasic Cu_2O-Cu catalyst. All these reports demonstrate superior activity of Cu, but they failed to break scaling relation and introduce new products such as C_4 chemicals. Since producing longer hydrocarbons can add more value to CO_2 reduction products.

Electrode	Potential vs. SHE V	Current density mA cm^{-2}	Faradaic efficiency, %							
			CH_4	C_2H_4	EtOH[a]	PrOH[b]	CO	$HCOO^-$	H_2	Total
Pb	−1.63	5.0	0.0	0.0	0.0	0.0	0.0	97.4	5.0	102.4
Hg	−1.51	0.5	0.0	0.0	0.0	0.0	0.0	99.5	0.0	99.5
Tl	−1.60	5.0	0.0	0.0	0.0	0.0	0.0	95.1	6.2	101.3
In	−1.55	5.0	0.0	0.0	0.0	0.0	2.1	94.9	3.3	100.3
Sn	−1.48	5.0	0.0	0.0	0.0	0.0	7.1	88.4	4.6	100.1
Cd	−1.63	5.0	1.3	0.0	0.0	0.0	13.9	78.4	9.4	103.0
Bi[c]	−1.56	1.2	-	-	-	-	-	77	-	-
Au	−1.14	5.0	0.0	0.0	0.0	0.0	87.1	0.7	10.2	98.0
Ag	−1.37	5.0	0.0	0.0	0.0	0.0	81.5	0.8	12.4	94.6
Zn	−1.54	5.0	0.0	0.0	0.0	0.0	79.4	6.1	9.9	95.4
Pd	−1.20	5.0	2.9	0.0	0.0	0.0	28.3	2.8	26.2	60.2
Ga	−1.24	5.0	0.0	0.0	0.0	0.0	23.2	0.0	79.0	102.0
Cu	−1.44	5.0	33.3	25.5	5.7	3.0	1.3	9.4	20.5	103.5[d]
Ni	−1.48	5.0	1.8	0.1	0.0	0.0	0.0	1.4	88.9	92.4[e]
Fe	−0.91	5.0	0.0	0.0	0.0	0.0	0.0	0.0	94.8	94.8
Pt	−1.07	5.0	0.0	0.0	0.0	0.0	0.0	0.1	95.7	95.8
Ti	−1.60	5.0	0.0	0.0	0.0	0.0	tr.	0.0	99.7	99.7

Table 1.2 Various metal electrodes and their CO_2 reduction products. Faradaic efficiencies of each product are indicated.

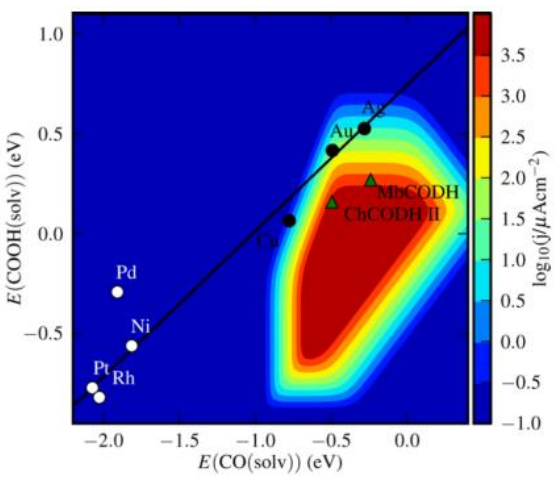

Figure 1.4 Kinetic volcano plot for CO evolution at a 0.35 V overpotential from the (211) step of transition metals.

Surface	T-mode[a] energy/meV	Relative amplitude[b]	CO adsorption energy/kJ mol^{-1}
Cu(1 1 1)	4.07	1.00	47.3
Cu(1 0 0)	3.94	1.03	51.1
Cu(1 1 0) parallel to step edge	3.75	1.09	54.0
Cu(1 1 0) perpendicular to step edge	3.40	1.20	54.0
Cu(2 1 1)	3.00	1.36	58.4
Cu(5 1 1)	3.05	1.33	57.7
Sputtered on Cu(1 0 0)	3.20–2.52	1.27–1.62	58.2

Table 1.3 The frustrated translational vibration energy of adsorbed CO on copper

1.3.3 Advantages of producing long carbon-chain hydrocarbons

As an effort to overcome energy crisis, development of catalysts which can produce long carbon-chain hydrocarbons is necessary. We envision that electroproduction of long chain hydrocarbons may significantly impact fossil fuel based current industry, because those chemicals have similar energy contents as that of gasoline (Table 1.4) [29]. Especially, n-butanol has energy density of 26.9 MJ/L, which is larger and closer to gasoline (30~33 MJ/L) than ethanol (21.4 MJ/L). n-butanol, a potential fuel substitute to displace gasoline, is being tested as a candidate for the mixing material with gasoline in the U.S. The fuel 1) is about seven times less evaporative, 2) has high compatibility with current infrastructure, 3) has low hygroscopicity amenable for pipeline distribution and 4) can be used a lot in industry (solvent, feedstock, plastics, paints, adhesives, cleaning products, etc). Therefore, researches on developing new catalysts which are capable of reducing CO_2 into n-butanol should be conducted.

Table 1. Comparative fuel characteristics.[26,54]

	N-butanol	Isobutanol	Ethanol	Gasoline
Energy density (MJ/L)	26.9	26.6	21.4	30–33
LHV (MJ/kg)	33.2	33.1	26.8	41–44
Research octane number	96	106	110	88–98
Motor octane number	84	90	90	80–88
Heat of evapo-ration (MJ/kg)	0.71	0.69	0.92	0.36
Reid vapor pressure (kPa)	2.2	3.3	16	54–103
Boiling point (°C)	117.7	107.9	78	27–225
Solubility at 20°C			miscible	negligible
% wt in water	7.7	8.7		
% wt water in	20.1	20		

Table 1.4 Comparative fuel characteristics of n-butanol, isobutanol, ethanol and gasoline

1.4 Design of new catalysts

1.4.1 Clues from nature

An important lesson for the improvement of catalytic ability of Cu electrode can be achieved from nature. Unlike sequential chain addition from C_1 to C_2 and to C_3 suggested by Prof. Jaramillo (Figure 1.5)[8], in synthetic approach, biological pathway, employed in genetically engineered bacteria, makes C_4 chemical that is produced by coupling of two C_2 intermediates and acts like building block for C_{4n} polysaccharide (Figure 1.6)[30–32]. In detail, acetyl group is attached to enzyme, so called CoA, and continuous formation of disulfide bridge between two acetyl–CoA species brings two acetyl groups close, triggering Claisen condensation to make butyl group. Similarly, resulting C_4 chemicals are utilized to produce C_8, C_{12} and so on, through the condensation reaction, without electron involvement[33]. Inspired by the biological mechanism, we conceive that synthetic inorganic catalysts that use C_2 or C_4 building blocks for butanol formation and further condensation yielding longer hydrocarbon chain may exist.

In addition to C_2 coupling mechanism, alloying can be another key bioinspired method to improve Cu electrode. Carbon monoxide dehydrogenase (CODH) is a well-known enzyme for the reduction of CO_2 (Figure 1.7)[34]. Active site of the enzyme is Ni-Fe cluster as shown in inset of Figure 1.7. Carbon dioxide can bind to the active site, between Ni and Fe, and the difference of redox potentials of Ni and Fe cause efficient breakage of C-O bond. Usually, Ni and Fe are known to produce hydrogen over CO_2 reduction products[11], but combining them together in an enzyme increased its catalytic activity. From this example, it can be concluded that alloying Cu with another heterogeneous atom might reinforce hydrocarbon converting characteristic of Cu electrode. The fact that alloying can change coordination of CO_2 on the surface backs up the hypothesis.

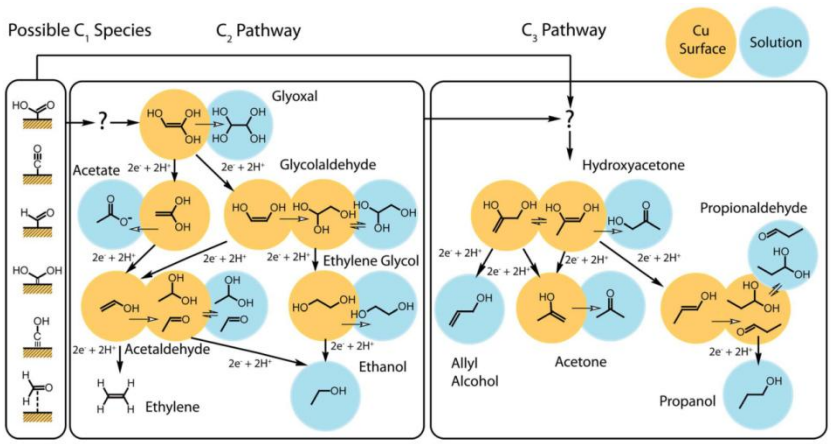

Figure 1.5 Proposed mechanism for C_2 and C_3 chemicals. C–C chain growth was explained by sequential addition of C_1 chemicals.

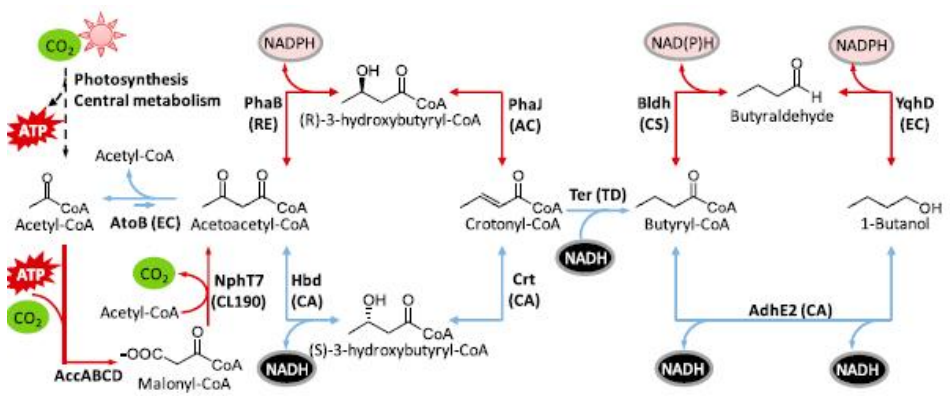

Figure 1.6 CoA-dependent 1-butanol pathway. The fermentative CoA 1-butanol pathway is in blue. Alternative routes are in red. EC, *E. coli*; RE, *R. eutropha*; CA, *C. acetobutylicum*; AC, *A. caviae*; TD, *T. denticola*; CS, *C. saccharoperbutylacetonicum* N1-4; *CL190*, *Streptomyces* sp. strain CL190.

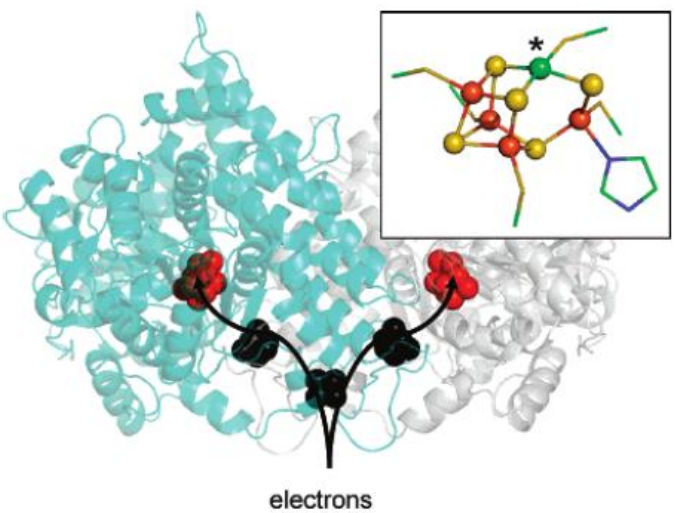

Figure 1.7 3D structure of carbon monoxide dehydrogenase (CODH) and its Ni-Fe cluster

1.4.2 Cu-based amorphous binary alloy

To use Cu-based alloy electrodes for electrochemical CO_2 reduction as a proof of concept, we investigated Cu-Ti binary system. Cu is known to have moderate binding affinity for carbon oxygenate preferentially through carbon-Cu bridge that can be explained by completely filled d-band structure and resulting occupancy of anti-bonding states[35]. Ti is representative oxophilic element that can make both monodentate and bidentate bonds with CO_2 and can prolong residence time for adsorbed intermediates, increasing their surface coverage[36]. It was also known that two acetaldehyde molecules can undergo Aldolization to produce a C_4 chemical on the surface of TiO_2 (Figure 1.8)[37]. Therefore, combining Cu, which has great hydrocarbon conversion rate, with Ti, which has ability to couple two C_2 chemicals, can lead to production of C_4 chemicals by electrochemical reduction of CO_2.

In defined crystal framework of synthetic catalysts, forming catalytic active sites with homogeneous local atomic symmetry, it seems impossible to precisely control such a complicated reaction pathway. In crystalline alloy, compositional effect usually tunes the catalytic activity by homogeneously modifying the catalyst surface with preserving the scaling relation (Figure 1.9 and Figure 1.10)[20,26].

One promising idea is breaking crystal symmetry, hopefully to find a new reaction pathway that cannot be observed in currently available crystals. Amorphous alloy, a key innovation reported here, can serve as an unprecedented platform to simultaneously tune atomic configuration and its composition, imposing a symmetrical heterogeneity to the catalyst surface as well as modifying its chemical properties, which can eventually overcome an intrinsic limitation of the scaling relationship[38–40]. The overall research scheme is shown in Figure 1.11.

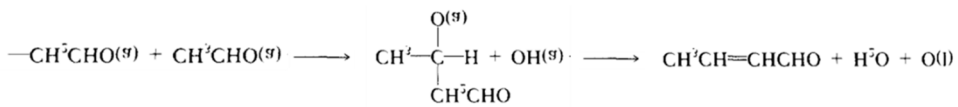

Figure 1.8 Aldolization of acetaldehydes on the surface of TiO_2.

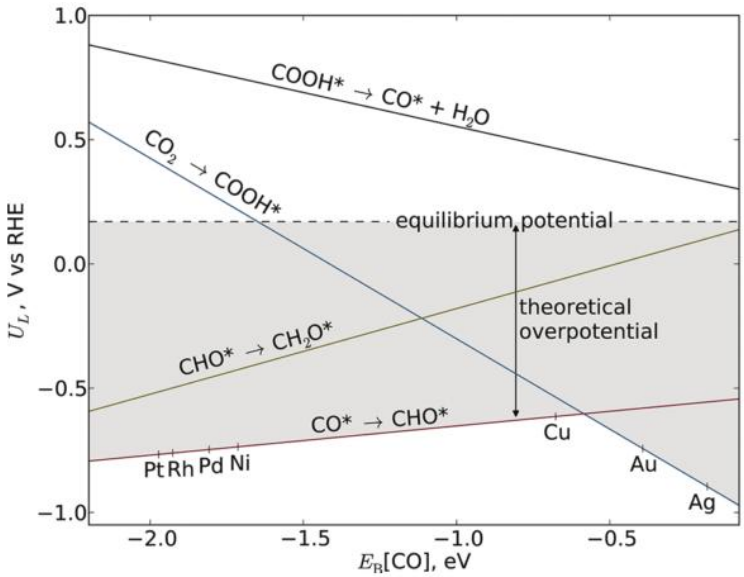

Figure 1.9 Limiting potentials (UL) for elementary proton−transfer steps

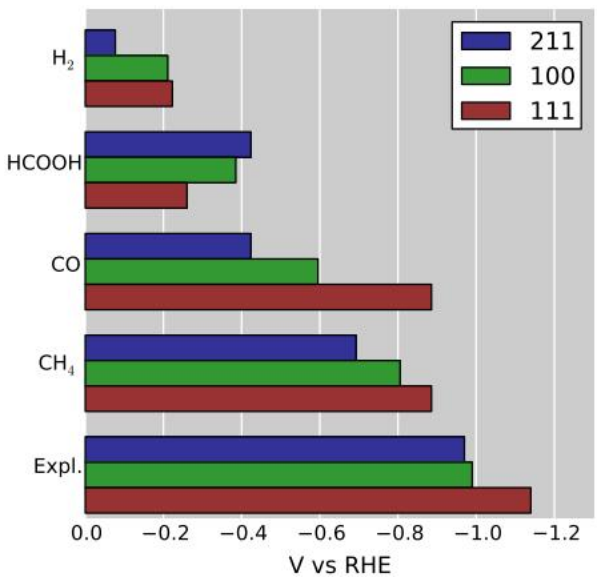

.

Figure 1.10 Facet dependence of product selectivity on Cu (211), Cu (100) and Cu (111) electrode.

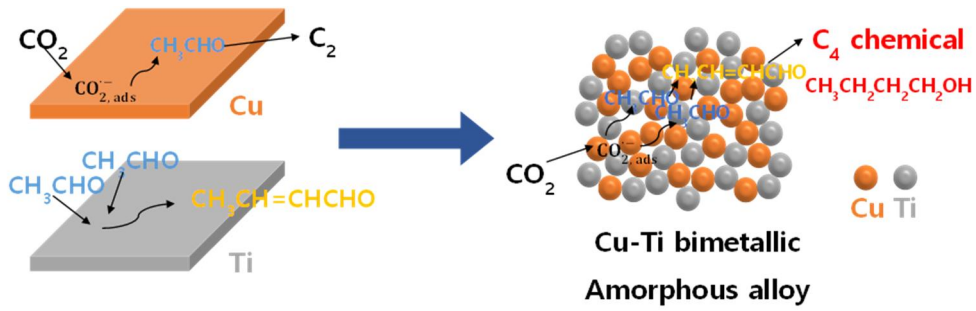

Figure 1.11 Overall research scheme

Chapter 2. Introduction

2.1 Preparation of amorphous Cu-Ti alloy

In this work, amorphous alloys were fabricated by melt spinning method. Among compositions inside the amorphous region for Cu-Ti binary system, three compositions were chosen (Cu : Ti = 60:40, 50:50, 40:60). $Cu_{60}Ti_{40}$, $Cu_{50}Ti_{50}$ and $Cu_{40}Ti_{60}$ alloy ingots were produced by arc-melting Cu, Ti metals under a Ti-gettered argon atmosphere in a water cooled copper crucible. Rapidly solidified ribbon samples were prepared by re-melting the alloy ingots in quartz tubes, followed by ejecting with an over pressured of 50 kPa through a nozzle onto a copper wheel rotating with a surface velocity of 40 m/s. This surface velocity corresponds to 3000 rpm. The resulting ribbons have a thickness of 30 μm and a width of 3 mm.

2.2 Characterization

2.2.1 X-ray Diffraction (XRD)

Phases were identified with X-ray diffraction (XRD) data collected on a Bruker D8 ADVANCE X-ray diffractometer with Cu K_{α} 1 radiation (wavelength (λ) : 1.5418 Å). Samples were loaded on a Si holder, retrofitted in X-ray diffractometer. XRD patterns of manganese oxide materials were recorded in a range of 20~80° with a step of 0.01° and a velocity of 1°/min. Obtained XRD patterns were compared with previously reported JCPDS cards.

2.2.2 Transmission Electron Microscopy (TEM)

Transmission electron microscopy (TEM) images and selected area electron diffraction (SAED) patterns were taken by using a high resolution transmission electron microscope (JEM-2100F, JEOL, Japan) with an acceleration voltage of 200 kV. TEM samples were prepared by focused ion beaming (FIB) after attaching amorphous alloy samples on carbon coating.

2.2.3 CO_2-Temperature-programmed desorption (TPD)

CO_2-Temperature programmed desorption (TPD) is monitored by catalyst analyzer Belcat-B. 20 mg of each sample were loaded and pretreated in He for 2 hours at 250° C and then cooled down to room temperature. The CO_2 flow were introduced into the cell for 2 hours to adsorb CO_2 on surface and then residual CO_2 and weekly physisorbed CO_2 were washed out with He flow for 1 hour. The CO_2 desorption is monitored with a ramping rate of 10° C/min under He up to 600° C.

2.2.4 Differential Scanning Calorimetry (DSC)

Differential scanning calorimetry (DSC) is conducted to verify amorphous structure of fabricated amorphous alloy samples. A pan with diameter less than 5 mm is filled with amorphous alloy samples. Samples are cut into small pieces and total mass of pieces are measured (usually 10~20 mg). Two pans, one with samples and a blank one as a reference, were placed in the equipment and temperature was raised from 400 to 850 K at a rate of 40 K/min. Then heat flow of both pans was measured with DSC.

2.3 Electrochemical analysis

All the electrochemical measurement were performed in a three-electrode electrochemical cell system. Ag/AgCl reference electrode (in 3 M KCl) and Pt foil (2 cm × 2 cm × 0.1 mm, 99.997 % purity, Alfa Aesar) are used as the reference electrode and counter electrode, respectively. Following electrochemical experiments were conducted by using a potentiostat system (CHI 600D, CH instruments). The electrolyte in all experiments was 0.1 M $KHCO_3$ in deionized water unless cited. The electrolyte is degassed by bubbling with high-purity Ar (99.99%) before the start of each experiment then purged with high-purity CO_2 (99.99%) for at least 30 minutes. Before each experiment, electrodes were electropolished by sweeping 100 cycles from 0.0 V to −2.5 V (vs. Ag/AgCl) for reliable measurements and clean surfaces at a scan rate of 0.1 V/s. It also had to be clear rougher surface (less shiny surface) of the electrode faces toward the counter electrode. All the data were iR-compensated with the resistance which was recorded before experiments. ($V = V_{applied} - iR$) Electrode potential, measured with Ag/AgCl reference electrode, was converted to the NHE scale afterwards, using the following equation :

$E(NHE) = E(Ag/AgCl) + 0.197\ V - iR$

2.3.1 Electrode preparation

To prepare working electrodes for electrochemical experiments, synthesized amorphous alloy ribbons were cut into 1.5 cm long pieces by scissors. Copper tapes were attached to one end of pieces to successfully conduct electric current. After setting up electrochemical cell for experiment, approximately 1 cm of the electrode will be placed inside electrolyte, thus keeping reaction area to 0.6 cm^2.

2.3.2 Linear Sweep Voltammetry (LSV)

Linear sweep voltammetry (CV) is an electrochemical measurement used to explore electrocatalytic performance of electrodes. In linear sweep voltammetry experiment, applied potential to the working electrode changes in a constant rate, which is called scan rate. When the potential applied to the working electrode reaches the final potential, the experiment does not continue and the current at the working electrode is plotted against the applied potential. In the work, potential range was set from 0 to – 2.5 V (vs. Ag/AgCl). All LSV measurements were conducted with

scan rate of 0.1V/s. Before each experiment, it was necessary to check whether resistance of the electrochemical system is constant. Usually, resistances are in the range of 20~60 ohm. If resistance is too high (> 100), all the contacts should be tested once more and it has to be clear that copper tape does not sink into the electrolyte.

2.3.3 Bulk Electrolysis (BE)

Bulk electrolysis, also known as controlled potential coulometry or potentiostatic, is an electrochemical method which applies constant potential to the working electrode over time. In this experiment, current flowing through the working electrode is measured over an interval. In this research, bulk electrolysis was used to monitor reaction products and their Faradaic efficiencies at a specific potential. Potential range from −1.4 V to −2.5 V (vs. Ag/AgCl) was applied until total charge passed through the working electrode reaches 5 C.

2.4 Product analysis

2.4.1 Gas Chromatography (GC)

The gas products are quantitatively analyzed by flame ionization detector gas chromatography (FID-GC, PerkinElmer, NARL8502 Model 4003) equipped with an active-carbon-packed column (6' HayeSep N 60/80 SF, carrier gas: Ar) at 120 °C. One milliliter of the gas is injected into the FID-GC by a syringe at the designated time. The molar proportion of the products relatively is measured by FID-GC and the exact amount of gas is calculated by multiplied by the head space of the reactor. The moles of products evolved during electrolysis is calculated from the integrated area of the product peaks in the gas chromatogram using 0.1 mol% standard gas.

2.4.2 Head Space Gas Chromatography Mass Spectrum (HS-GC-MS)

The mass of the products were confirmed by head space gas chromatography mass spectrum (HS-GC-MS, Agilent, 7890A GC/5977A MS) using a quadrupole-type mass spectrometer and

HP-PLOT molesieve capillary column (Agilent). Typically, electrolyte after bulk electrolysis is carefully transferred to 20 ml of cramp type headspace vial. Then 100 μL of the gas is injected into the GC-MS by an auto sampler after evaporated the liquid product for 5 minutes. The mass of products are analyzed after segregation by a gas chromatograph.

2.4.3 Nuclear Magnetic Resonance (NMR)

Liquid phase products are quantified using 1D ^{1}H-NMR (600MHz, High Resolution NMR Spectrometer, Bruker, AVANCE 600). NMR analyses of all possible products are conducted to set standards by dissolving purchased chemicals in 0.1M $KHCO_3$ aqueous solution. DMSO is used as an internal standard. The strong water signal had to be suppressed by using the solvent presaturation procedure. In NMR measurement, parameters are identically set for all experiments (with a 0.5s prescan delay, 5s presaturation of the H_2O resonance, 45 degree read-pulse, over an 8000 Hz spectral width, 4s acquisition time, centered on the water peak, for 52 scans). NMR samples are made by mixing 600 μL of the electrolyte after bulk electrolysis with CO_2 reduction products and 30 μL of 10mM dimethylsulfoxide (DMSO) as an internal standard in D_2O. The

concentration of reaction products are measured from the ratio between integrated peak areas of products and DMSO.

2.4.4 Ultraviolet-Visible Spectroscopy (UV-Vis)

Ultraviolet-visible spectroscopy is an equipment for detecting absorption or reflectance in ultraviolet region. Thermo Scientifi c NanoDrop 2000c UV-Vis Spectrophotometer was used for the experiment. To measure absorbance, about 0.5~1 mL of the electrolyte should be placed inside a cuvette, so that there is sufficient amount of liquid for light to pass through.

2.4.5 High Performance Liquid Chromatography (HPLC)

High performance liquid chromatography (HPLC, Ultimate 3000, Dionex) was another technique used to analyze liquid products. For this experiment, Aminex 87H column (300*10mm, Bio-rad, USA) and RI detector (ERC, RefractoMAX520, Japan) and UV 210nm were used. For the mobile phase, 0.01N H_2SO_4 was used with the flow of 0.5mL/min at an oven temperature of 40 ℃. Only 10uL of the electrolyte was needed for the experiment.

2.4.6 Faradaic Efficiency (F.E.)

The Faradaic efficiency of a product is calculated by dividing the coulombs used to produce each chemical with the total coulombs supplied to the electrode during bulk electrolysis. Coulombs used to produce each chemical can be achieved by multiplying amount of produced chemical in moles, electrons required to produce one molecule from CO_2 and the charge of one electron. Total coulombs supplied to the electrode can be monitored after bulk electrolysis by a potentiostat. Usually, 5 C was passed through the working electrode.

Chapter 3. Results and Discussion

3.1 Characterization of Cu-Ti amorphous alloys

3.1.1 Verification on amorphous nature of samples

The amorphous Cu-Ti alloys were prepared by melt spinning method and the successful synthesis of amorphous electrodes was confirmed by X-ray diffraction (XRD) spectra, high resolution transmission electron microscopy (HR-TEM) and differential scanning calorimetry (DSC). It was previously reported that amorphous alloys of Cu-Ti bimetallic system can be formed well only ratio between two elements lie in a specific region called amorphous region (Figure 3.1)[41]. Thus, we fabricated alloys whose compositions are included in this region.

At first, we performed XRD analysis to confirm amorphous nature of Cu-Ti alloy samples (Figure 3.2). Alloys with various compositions (Cu : Ti = 30:70, 35:65, 40:60, 45:55, 50:50, 54:56, 58:42, 61:39, 65:35) were tested. When atomic concentration of Cu ranges from 30% to 70%, broad peaks were observed from XRD spectra. These broad peaks implies the fact that there are no

crystalline planes inside alloys. When atomic concentration of Cu in an alloy exceeded 70%, it easily became crystalline and the Cu_3Ti or Cu_4Ti phases were detected; the Ti_2Cu phase was observed in the alloys with Cu concentration less than 30%. However, XRD analysis can only show bulk nature of samples. Therefore, there is possibility that some crystalline phases could be formed on the surface, which is thermodynamically unstable region. Further study was need to clearly decide the crystallinity of fabricated samples.

As a next step, we used transmission electron microscopy (TEM) to precisely verify phases of $Cu_{40}Ti_{60}$ electrode. As shown in Figure 3.3, long-range order, corresponding to crystalline structure, was not observed. Same results were achieved with high-resolution TEM (HR-TEM) images. Additionally, ring shapes from selected area electron diffraction (SAED) implies the fact that no crystalline structure exists inside the electrode. Therefore, we could conclude that $Cu_{40}Ti_{60}$ electrode has amorphous phase, as we expected.

In addition to XRD and TEM results, differential scanning calorimetry (DSC) were conducted to gain another evidence that fabricated electrodes were amorphous alloys. Amorphous alloys exhibit typical shape of curves from DSC. These shapes were clearly shown in Figure 3.4. Even though $Cu_{40}Ti_{60}$ sample does not exhibit clear T_g on the curve, it is reasonable because Cu-Ti bimetallic system has poor amorphous formability at the

composition. Therefore, these results verified amorphous nature of samples once more.

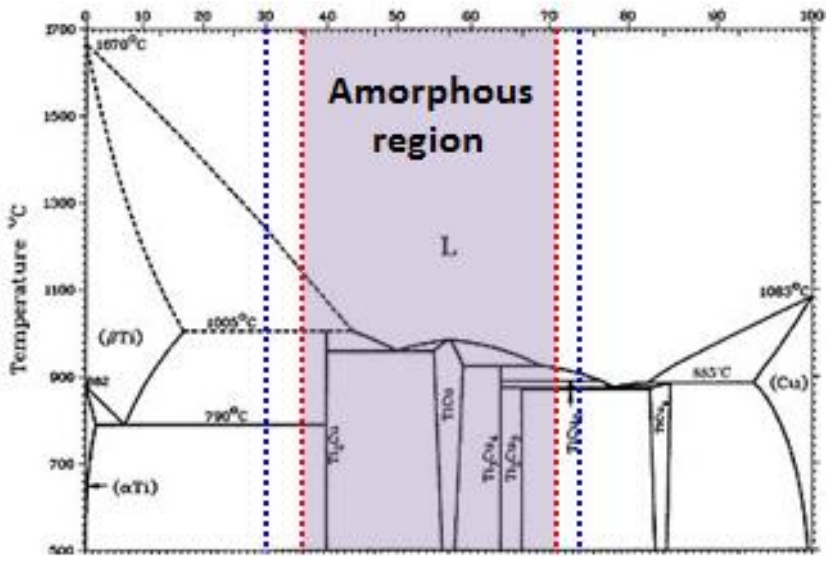

Figure 3.1 Phase diagram of Cu–Ti binary system. Amorphous region is depicted in the diagram according to previous works.

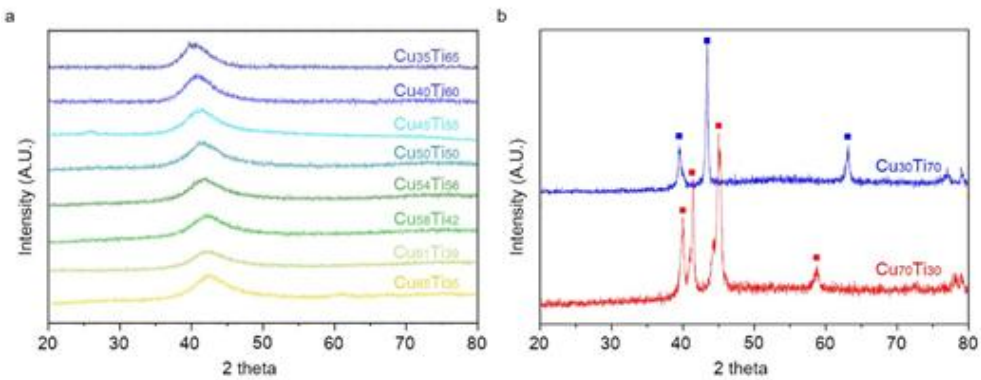

Figure 3.2 XRD spectra of a) amorphous Cu-Ti alloys with Cu composition ratio between 35 and 65, and b) crystalline Cu-Ti alloys when Cu composition of is more than 70% (red) and that of less than 30% (blue). Blue dot indicates Ti_2Cu phase, while red one does Cu_3Ti or Cu_4Ti phases.

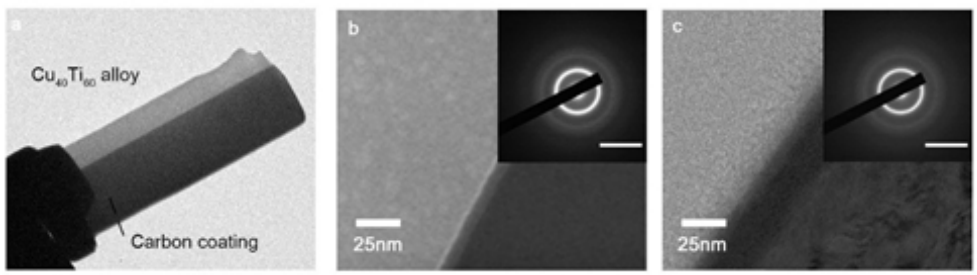

Figure 3.3 Transmission electron microscopy (TEM) image of amorphous $Cu_{40}Ti_{60}$ electrode. a) TEM image of amorphous $Cu_{40}Ti_{60}$ alloy. The sample was prepared by focused ion beam etching. b), c) High resolution TEM image of amorphous $Cu_{40}Ti_{60}$ electrode before and after electrolysis. The selected area electron diffraction (SAED) pattern of the observed area is depicted in the inset.

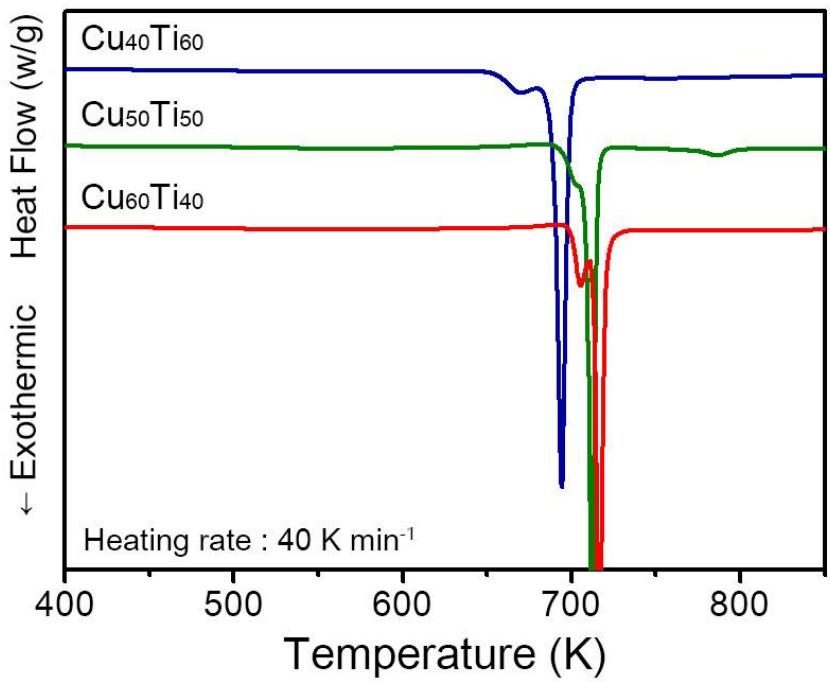

Figure 3.4 DSC curve of as-spun $Cu_{40}Ti_{60}$, $Cu_{50}Ti_{50}$, $Cu_{60}Ti_{40}$ electrodes

3.1.2 Electrocatalytic performance of electrodes

The electrocatalytic performances of the Cu–Ti alloys were evaluated via linear sweep voltammetry (LSV) in a CO_2–saturated 0.1M $KHCO_3$ aqueous solution. For this experiment, $Cu_{40}Ti_{60}$, $Cu_{50}Ti_{50}$, $Cu_{60}Ti_{40}$ alloy samples were used. All of electrochemical experiments were performed in one–compartment cell with controlled working electrode surface area (0.6 cm^2) and electrolyte volume (1 mL). For CO_2 environment, the electrolyte was saturated with CO_2 by bubbling for 30 min and the cell was purged by flowing CO_2 at less than 1 bar of pressure for another 15 min before sealing gas–tightly. Onset potential was defined as the potential required to reach current density of 1 mA cm^{-2}. Amorphous Cu–Ti electrodes exhibited enhanced catalytic activity as the Ti concentration increased. As shown in Figure 3.5, $Cu_{60}Ti_{40}$, $Cu_{50}Ti_{50}$ and $Cu_{40}Ti_{60}$ electrodes had onset potentials of −1.52 V, −1.46 V and −1.08 V, respectively, whereas, polycrystalline Cu did at −1.26 V. $Cu_{40}Ti_{60}$ electrode exhibited improved current density and lower onset potential in CO_2 environment than in Ar environment (Figure 3.6). This result implies the fact that the electrode is active for the CO_2 reduction reaction. Even after subtracting partial currents used for hydrogen evolution, $Cu_{40}Ti_{60}$ electrode had the lowest applied

potential (−1.18 V) at a current of 1 mA cm^{-2}, leading to the same conclusion (Figure 3.7). Therefore, amorphous $Cu_{40}Ti_{60}$ electrode exhibited the best catalytic performance as a CO_2 reduction catalyst after electrochemical analysis.

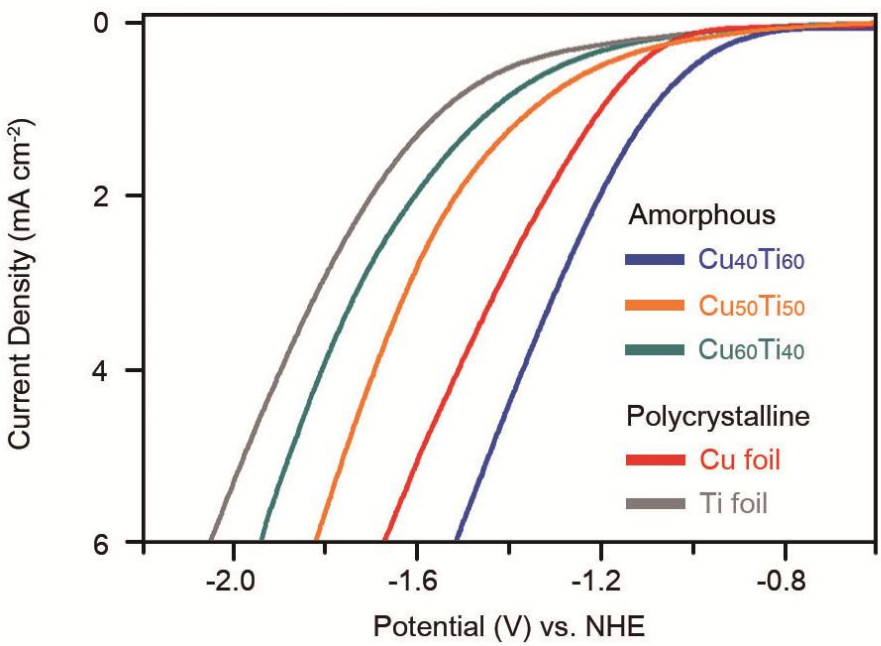

Figure 3.5 Linear sweep voltammetry (LSV) curves of Cu–Ti alloy in the amorphous phase with a composition ratio of $Cu_{40}Ti_{60}$ (blue), $Cu_{50}Ti_{50}$ (orange), $Cu_{60}Ti_{40}$ (dark cyan), polycrystalline Cu (red) and Ti (gray) foil in a CO_2 purged 0.1 M $KHCO_3$ aqueous solution.

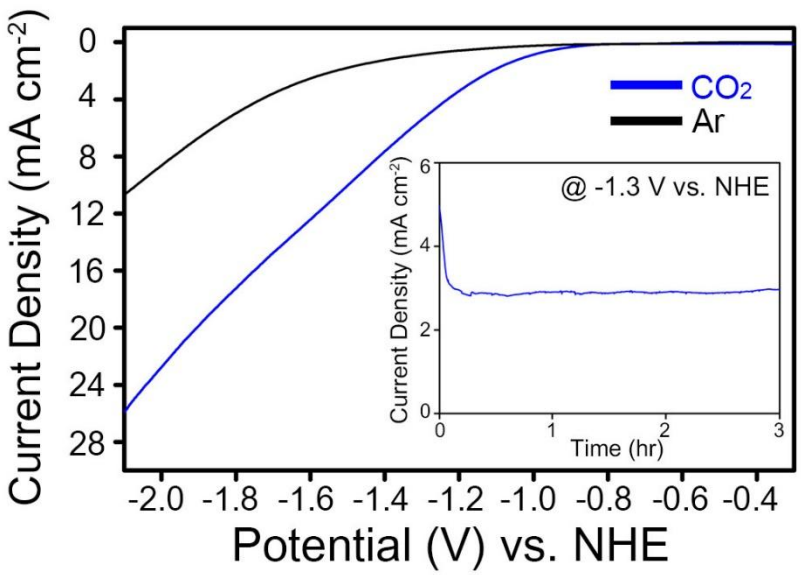

Figure 3.6 LSV curves for amorphous $Cu_{40}Ti_{60}$ electrode in CO_2 (blue) and Ar (black) environment. Plot for current density over time during bulk electrolysis is depicted in the inset.

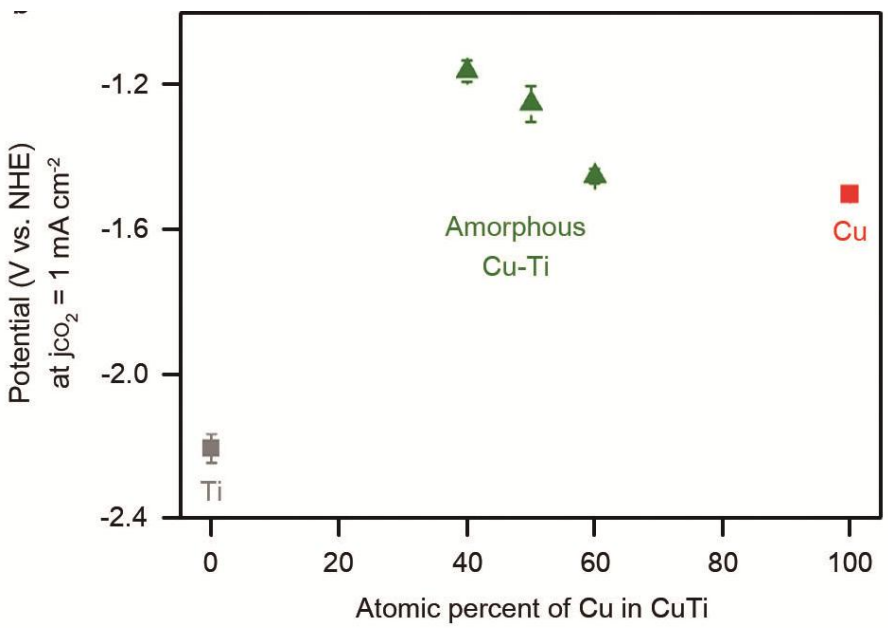

Figure 3.7 Applied potential to achieve 1 mA cm^{-2} of partial current density to reduce CO_2 depending on the composition of the electrode.

3.1.3 Effect of titanium concentration on catalytic performance

In order to discover the titanium concentration effect observed from Figure 3.7, adsorption energies of amorphous Cu-Ti electrodes for CO_2 were investigated by CO_2-temperature-programmed desorption (TPD). Figure 3.8 shows typical CO_2-desorption feature of polycrystalline Cu at 384 ° C and 443 ° C, which corresponds to moderate Lewis basic sites[42,43]. The amorphous Cu-Ti profiles exhibited similar characteristics; however, with increase of Ti content, a portion of the peak at 443 ° C was enhanced. Specifically, $Cu_{40}Ti_{60}$ had an additional binding mode, newly appeared at 523 ° C, that may correspond to strong Lewis basic site. According to previous research, pristine Ti has desorption peaks in temperature range −150 ° C to −50 °C[44]; thus the observed profiles were mainly from Cu. From the observed low overpotential and high CO_2 interaction, we performed product analysis, mechanism study and model reaction on $Cu_{40}Ti_{60}$ electrode.

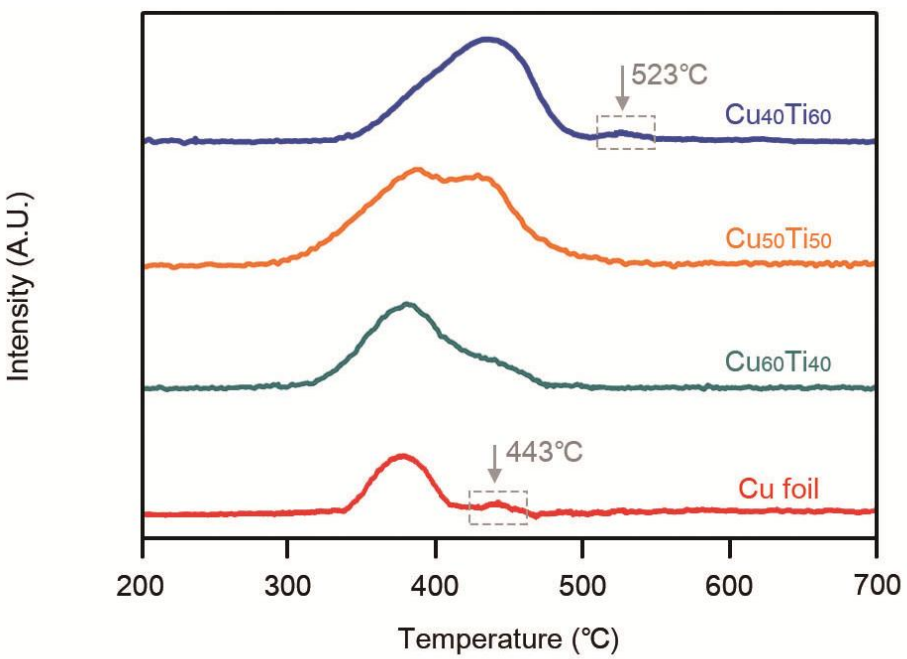

Figure 3.8 Temperature-programmed desorption (TPD) spectra of CO_2 at different composition ratios of an amorphous Cu-Ti electrode.

3.2 Product analysis after bulk electrolysis

3.2.1 Detection of n-butanol as a product

After electrocatalytic analysis, bulk electrolysis was conducted in a potential range from -1.4 V to - 2.5 V (vs Ag/AgCl) to accumulate sufficient amount of products for product analysis. Bulk electrolysis was performed to pass 5 C of electrons at potentials from −1.2 V to −2.3 V (vs. NHE). Product analysis at applied potential lower than −1.2 V was not conducted because of negligible amount of hydrocarbon formation. Final products and their Faradaic efficiencies were analyzed using gas chromatography (GC) and ^{1}H nuclear magnetic resonance (NMR) spectroscopy. For NMR analysis, 600 μL of electrolyte was mixed with 30 μL of internal standard (10 mM DMSO in D_2O) without purification. Note that, NMR signals of butanol in 0.1M $KHCO_3$ aqueous solution were negatively shifted by 0.14, without changing the peak shapes, compared to those of conventional organic solvents, such as DMSO, due to different shielding effects (middle graph in Figure 3.9). NMR references for all of possible products and intermediates in a 0.1M $KHCO_3$ solution were collected for exact peak assignments by matching chemical shift, intensity ratio, and splitting mode (Table

3.1). Additionally, standard curves of each chemical were made over concentration range of interest for quantitative measurements.

Remarkably, butanol was observed with Faradaic efficiency of 25%. Bulk electrolyzed solution exhibited ^{1}H-NMR peaks centered at 0.8 (triplet), 1.2 (sextet), 1.5 (quintet) and 3.5 (singlet) ppm, which were well-matched with the butanol reference. Based on the standard curves, quantification of butanol was conducted by comparing peak area with that of DMSO. This is the first time to report production of C_4 chemical (n-butanol) as a major product.

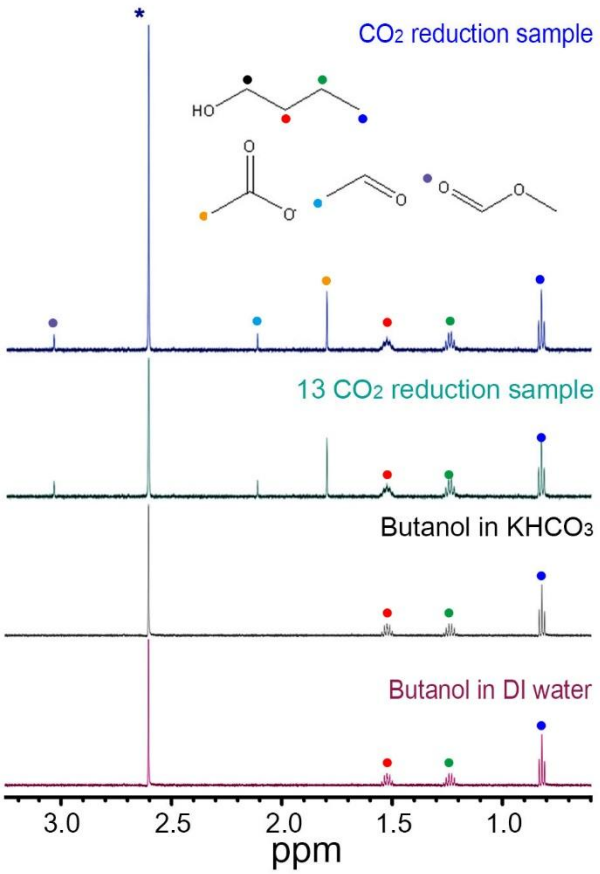

Figure 3.9 ^{1}H−NMR spectra of bulk electrolyzed sample at applied potential of −1.3 V vs. NHE. The origins of peaks are denoted by colored dots with corresponding molecular structure (asterisk indicates DMSO standard solution).

CO_2 reduction products			Assignment		$^{13}CO_2$ environment
Chemical Shift	^{1}H splitting	J coupling	Probed nucleus	Product Name	Chemical Shift
0.79	t	7.39	$CH_3CH_2CH_2CH_2OH$	n-butanol	0.68, 0.89
1.06	t	7.03	CH_3CH_2OH	ethanol	
1.2	d	5.26	$CH_3CH(OH)_2$	acetaldehyde	1.11, 1.31
1.24	sextet	7.44	$CH_3CH_2CH_2CH_2OH$	n-butanol	1.13, 1.35
1.52	quintet	7.9	$CH_3CH_2CH_2CH_2OH$	n-butanol	1.42, 1.62
1.79	s		CH_3COO-	acetate	1.68, 1.9
1.9	s		$CH_3C(=O)CH_2OH$	hydroxyacetone	
2.1	s		$CH_3CO=CH_3$	acetone	
2.12	d	3	$CH_3CH=O$	acetaldehyde	2.01, 2.18
2.6	s			DMSO	
3.0	s		$CH_3OCH=O$	methyl formate	2.88, 3.12
3.23	s		CH_3OH	methanol	
3.5	t	7.41	$CH_3CH_2CH_2CH_2OH$	n-butanol	3.38, 3.62
				water	

Table 3.1 Collected NMR library of CO_2 reduction products and intermediates.

3.2.2 Verification of synthesis of n-butanol

Butanol formation was further verified using gas chromatography-mass spectroscopy (GC-MS) (Figure 3.10). Mass spectrum exhibited signals at 31, 43, 56, 73 and 74, all of which corresponds to reported database[45]. Signal at 74 was a typical peak for molecular ion of butanol itself and rest peaks were assigned as fragments of ionized butanol. To confirm that butanol came from purged CO_2, bulk electrolysis was conducted in $^{13}CO_2$ environment and $H_2{}^{18}O$ solution (Figure 3.9). ^{1}H-NMR spectra of ^{13}C-labelled solution exhibited peaks at different chemical shifts and intensities, due to different electron densities of ^{13}C and ^{12}C. This reflects the presence of ^{13}C-butanol in the electrolyte, which is direct evidence that carbon source of butanol is CO_2 gas. The increase of ^{1}H-NMR peaks of n-butanol with increasing amount of charges passed through the working electrode also indicated that n-butanol was produced by electrochemical reaction inside the cell (Figure 3.11 a)). A clear linear relationship between the reaction time and produced amount of n-butanol is shown in Figure 3.11 b). When electrolysis was conducted in various $KHCO_3$ concentrations, partial current for reducing CO_2 did not change, indicating carbon source did not originate from HCO_3^- ion (Figure 3.12). Additionally, bulk

electrolysis in $H_2{}^{18}O$ under the equivalent reaction conditions also resulted in the same mass spectra as that of $H_2{}^{16}O$ (Figure 3.13). Thus, both C and O atoms in butanol solely originated from CO_2.

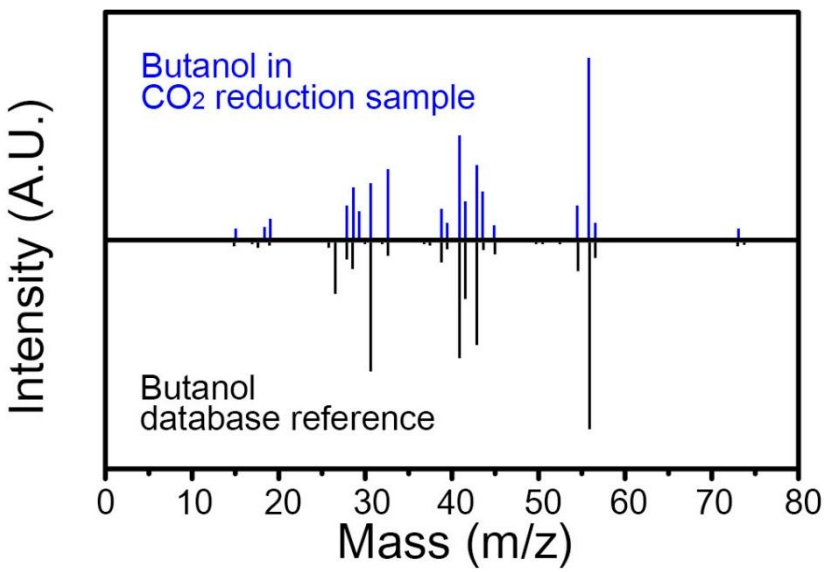

Figure 3.10 Headspace gas chromatography (HS-GC) mass spectra of produced butanol (black), compared to database reference mass spectrum (blue).

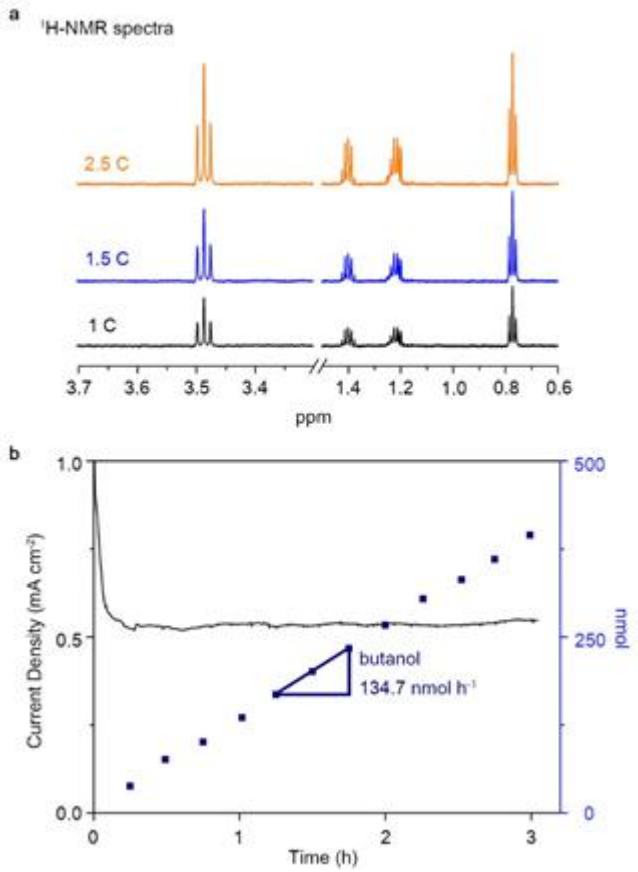

Figure 3.11 butanol formation in the course of electrolysis. a) Linear increase of butanol along with the reaction time observed in $^{1}H-NMR$ spectra. Each spectra are denoted with passed electron to produce butanol. b) Current density over the reaction time for amorphous $Cu_{40}Ti_{60}$ electrode at − 1.3V and moles of converted CO_2 for butanol (dark blue). Turn over number of each products are calculated based on their slopes.

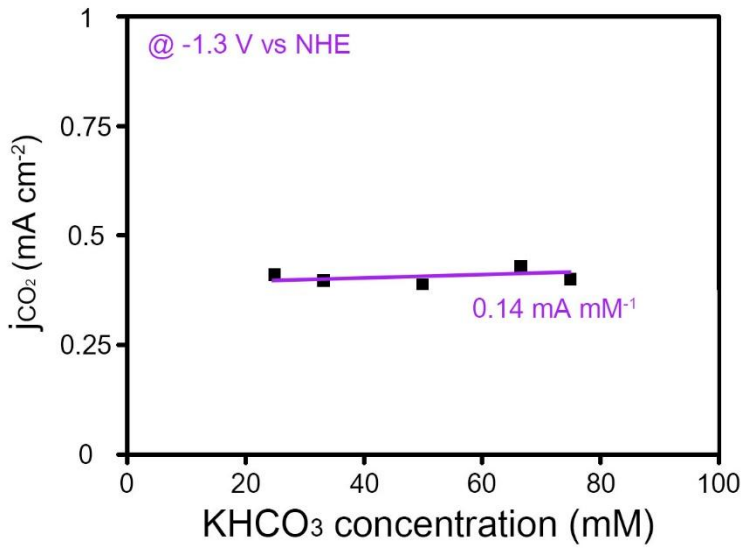

Figure 3.12 $KHCO_3$ concentration dependence on CO_2 reduction. $KHCO_3$ concentration dependence of steady-state catalytic current density at constant potential of - 1.3V vs. NHE. The total ionic concentration of the electrolyte was compensated with KCl to maintain 100 mM.

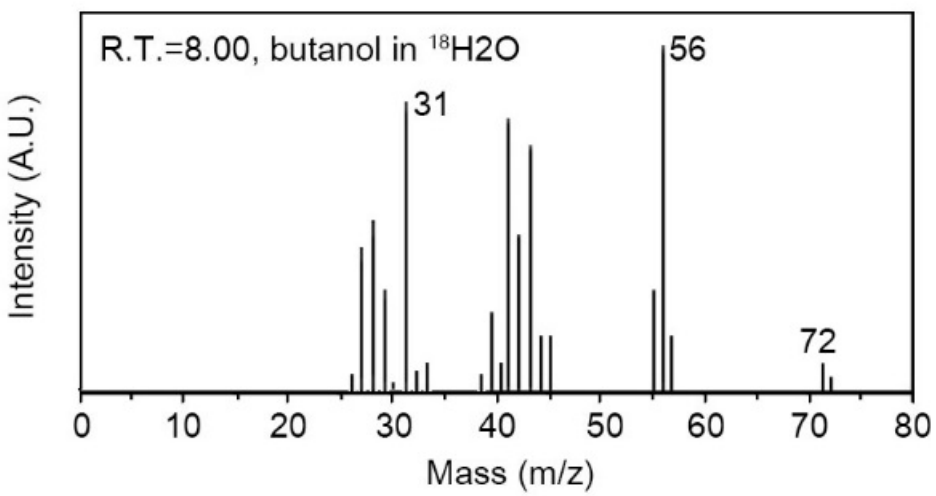

Figure 3.13 Mass spectra of synthesized butanol under $H_2{}^{18}O$ solution. The mass spectra of butanol synthesized from the bulk electrolysis in electrolyte with $H_2{}^{18}O$ under equivalent conditions.

3.2.3 Potential dependence of products

Faradaic efficiencies of all detected products were displayed against applied potential. As shown in Figure 3.14, CO_2 reduction dominated in low potential region, while hydrogen evolution did in high potential. At −1.2 V, 76.4% of total current was in charge of CO_2conversion and the rest was used for hydrogen evolution. Of CO_2 reduction outcomes, methyl formate, butanol and 1,1−dibutoxybutane were observed as major products with Faradaic efficiencies of 13.5%, 25% and 22%, respectively. It is worthwhile to mention that these products have not been observed in any other CO_2 reduction catalyst. As more negative potential was applied, acetaldehyde and ethylene were observed, exhibiting maximum efficiencies of 8.7% and 32.6% at potential of −1.4V and −1.8V, respectively. The production of acetaldehyde was confirmed by both ^{1}H−NMR and by Schiff' s reagent. (Figure 3.15) Butane was also clearly detected in potential range of −1.3 V to −2.0 V and its optimum Faradaic efficiency of 6.7% was observed at −1.6 V. However, in the same potential region, that of butanol steadily decreased and almost disappeared at −2.0 V. When potential increased above −2.0 V, hydrogen was mainly produced with over than 73.2% of selectivity. Observed products and their selectivity

trend depending on potential had both similarities and differences from that of polycrystalline Cu and other reported Cu-based alloys. When applied potential was higher than −2.0 V, exclusive hydrogen evolution was commonly observed. In moderate potential range of −1.5 V to −2.0 V, ethylene was obtained as major product with similar Faradaic efficiency of approximately 30%, however, optimum potential was negatively shifted approximately 400 mV from that of polycrystalline Cu[46]. In low potential range, below −1.5 V, there was a noticeable difference that formate, carbon monoxide and methane, typically observed as major products on polycrystalline Cu, were detected with Faradaic efficiencies of 0.7%, 2.1%, and 1.4%, respectively. More interestingly, unlike polycrystalline Cu, which generally evolves gas and soluble liquid products, $Cu_{40}Ti_{60}$ electrode produced white and insoluble precipitates, identified as 1,1-dibutoxybutane, after long-term bulk electrolysis.

Formation of 1,1-dibutoxybutane was verified by NMR and mass spectroscopy analysis. As shown in Figure 3.16, the precipitates were deposited on the electrode surface and the thickness steadily increased with reaction time. After approximately 9 hours, it can be easily observed by naked eye. ^{1}H-NMR spectra exhibited several peaks at 0.8, 3, 5.2 and so on, while ^{13}C-NMR did at 14.1, 32.5, 68.2 and so on (Figure 3.16 and Figure 3.17). In ^{1}H-NMR spectra,

triplet peak at 3 ppm indicates the precipitates contain ether bond[45]. Another triplet at 5.2 ppm reflects that electron withdrawing species are attached to a carbon chain, such as alkoxy group[45]. Based on doubled intensity of peaks observed at 14.1, 19, 32.5 and 68.2 ppm in ^{13}C-NMR spectra, we concluded these correspond to two butoxy chains. Mass spectra also exhibited signals at 57, 73, 131 and 159, which further confirms that the polymeric compound is 1,1-dibutoxybutane (Figure 3.17)[47]. From the fact that 1,1-dibutoxybutane is observed together with only butanol, we attempted to find a pathway starting from butanol. When butanol disappeared at potential higher than -1.8 V, 1,1-dibutoxybutane was not detected either. Another observation that helped us to propose mechanism was that butanal also exists as a minor product (Figure 3.18). Ether bond can be formed by nucleophilic attack of hydroxyl group on carbonyl group, called Acetal reaction[45]. Therefore, we propose that 1,1-dibutoxybutane is synthesized via Acetal reaction between two butanol and a butanal.

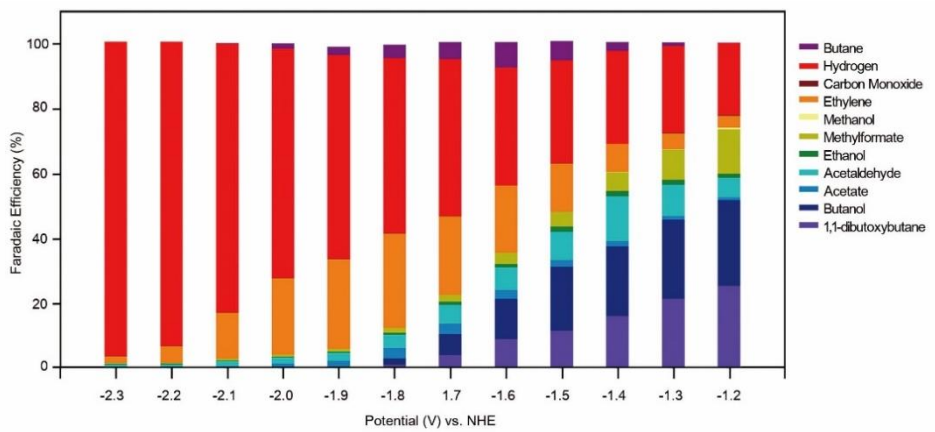

Figure 3.14 Overall chemical selectivity for CO_2 reduction in applied potential range of − 1.2 V to − 2.3 V. Products detected with chemical selectivity of less than 1 % are not displayed in chart.

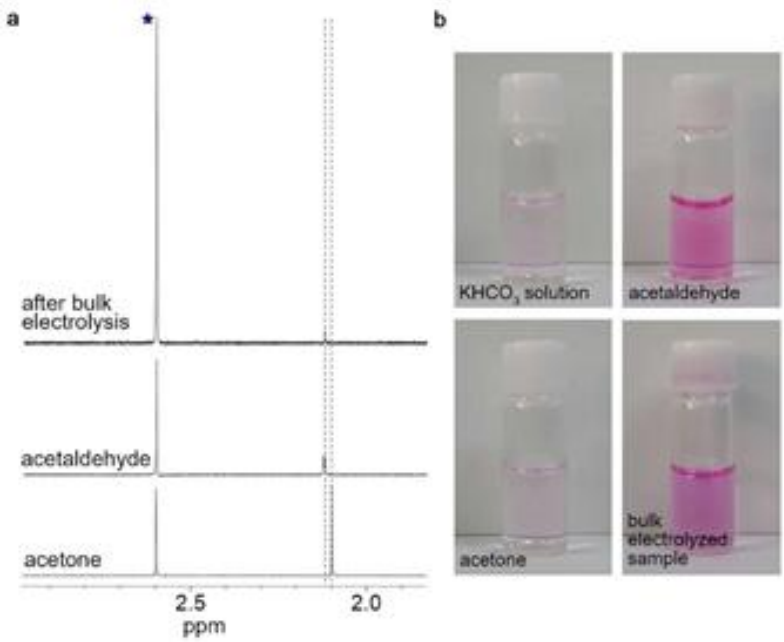

Figure 3.15 Confirmation of acetaldehyde as a reaction intermediate. a) ^{1}H–NMR spectra of bulk electrolyzed sample, acetaldehyde and acetone in the chemical shift range of 2.9 – 1.9 (asterisks indicate standard solution peaks; 10 ppm of DMSO). b) Color change after Schiff reaction. Red color indicates the solution contains aldehyde species. Only bulk electrolyzed sample and acetaldehyde containing solution turned red.

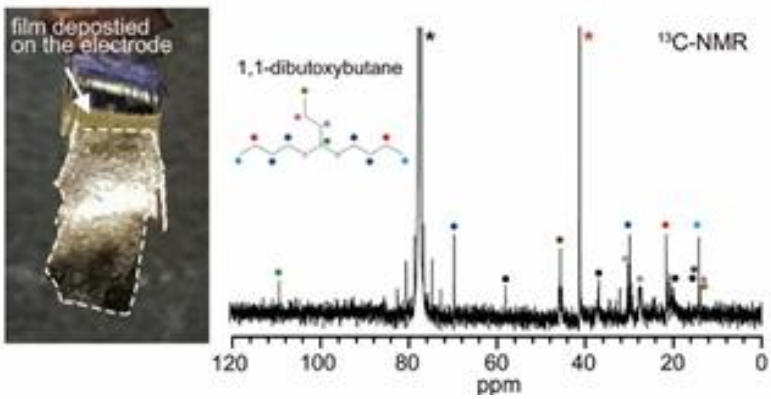

Figure 3.16 $^{13}C-NMR$ spectra of precipitated 1,1-dibutoxybutane. Observed peaks with significant intensity at 79 ppm corresponds to $CHCl_3$ solvent and is denoted by black asterisk, while, red asterisk denotes standard solution. NMR spectra of butanol and butanal are also observed and marked with black and gray dots. Picture of precipitates deposited on amorphous Cu-Ti (left).

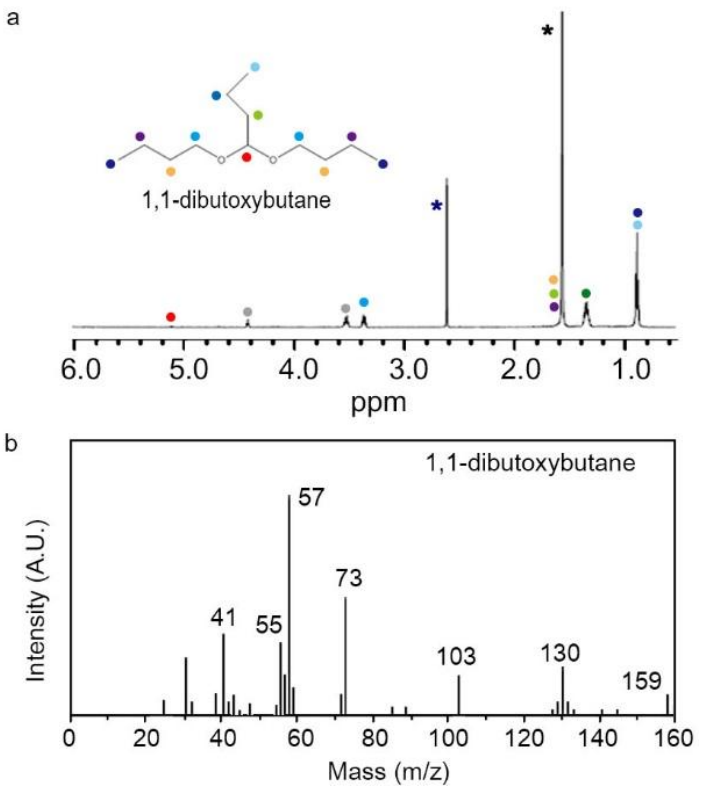

Figure 3.17 Confirmation of 1,1−dibutoxybutane as a CO_2 reduction outcome. a) ^{1}H−NMR spectra of 1,1−dibutoxybutane obtained at an applied potential of −1.3 V vs. NHE. Gray dots are peaks originated from butanol. b) GC mass spectra of 1,1−dibutoxybutane dissolved in the $CHCl_3$.

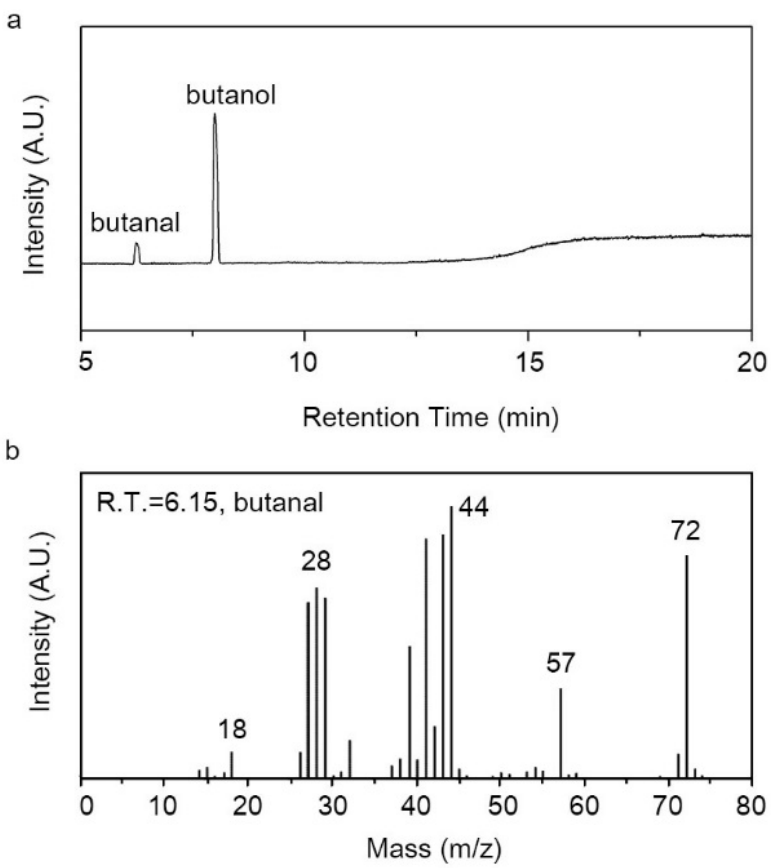

Figure 3.18 Gas chromatography analysis of detected reaction intermediates. a) gas chromatogram of bulk electrolyzed solution. b), c), Mass spectra of detected C_4 chemical, butanal.

3.3 Investigation on reaction mechanism

3.3.1 Possible reactions from C_2 intermediates

In order to design a new mechanism which includes the production of C_4 chemicals, it was necessary to investigate on possible reactions from C_2 intermediates such as methyl formate and acetaldehyde. In the field of molecular catalysis, it was shown that methyl formate can undergo isomerization on Ru^{II}—Sn^{II} heteronuclear cluster complex, $[Ru(SnCl_3)_5(PPh_3)]^{3-}$ [48]. A number of mechanism for isomerization of methyl formate to acetic acid have been proposed. They include (1) the decomposition of methyl formate to CH_3OH and CO, followed by carbonylation of methanol to acetic acid, (2) initial reaction with LiI promoter, which produced CH_3I and HCOOLi and (3) another mechanism which involves migration of methyl carbenium ion in the presence of Lewis acid. Unlike these mechanisms, methyl formate seems to be divided into C=O group and OCH_3 group for $[Ru(SnCl_3)_5(PPh_3)]^{3-}$ complex. Then the migration of C=O group to the other side of the molecule forms acetic acid. During this mechanism, some amount of CO can be detected due to the release of C=O group from the catalyst surface. All these mechanism provides evidences that methyl

formate can be isomerized into acetic acid in various mechanism and further reduction of acetic acid can produce acetaldehyde, another C_2 intermediate (Figure 3.19 a).

Another key intermediate observed by ^1H-NMR is acetaldehyde. As mentioned above, acetaldehyde was considered as an important intermediate during CO reduction[49]. Acetaldehyde is also proposed as a precursor for ethylene and ethanol in CO_2 reduction by Jaramillo group[8]. A noticeable characteristic of aldehydes is that they can react with themselves to synthesize larger molecules, and this is also true for acetaldehyde. When an acetaldehyde is transformed to ethenol by Keto-enol Tautomerism, this chemical reacts another molecule of acetaldehyde to form a chemical with four carbons, 3-hydroxybutanal. This reaction is called Aldol reaction between aldehydes[45]. Interestingly, this reaction resembles previously mentioned reactions which synthesizes n-butanol with genetically modified bacteria by Claisen condensation reaction in the field of synthetic biology. Although actual reactions are different, we could suggest that similar C_2 coupling reaction occurs in our system. Since acetaldehyde was detected as a product, we proposed that Aldol reaction might participate in the C_4 mechanism. Once 3-hydroxybutanal is formed, it can easily be reduced to n-butanol under reductive environment. Therefore, by looking at key intermediates and their possible relations, we could propose that

methyl formate can transform into acetic acid by isomerization. In reductive condition, acetaldehyde can be formed easily from acetic acid. Then Aldol reaction combines two acetaldehyde molecules and produces 3-hydroxybutanal, a C_4 chemical. Finally, 3-hydroxybutanal is further reduced to n-butanol. However, since this is only a suggestion, each step should be confirmed properly by designing model reactions.

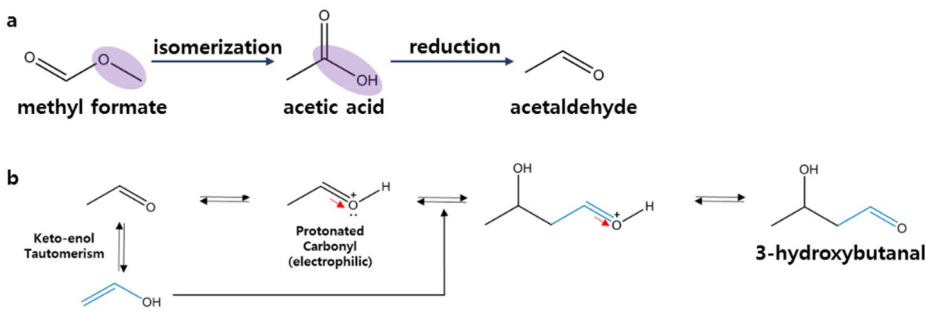

Figure 3.19 Possible reactions from C_2 intermediates. a) Isomerization of methyl formate to acetic acid and to acetaldehyde and b) Aldol reaction of acetaldehyde

3.3.2 Design of model reactions and proposal of C_4 mechanism

To propose reaction mechanism, we performed several model reactions that would proceed with experimentally identifiable intermediates and analyzed each step by verifying whether the intermediate can contribute to butanol formation. In low potentials range, where butanol and 1,1-dibutoxybutane were major products, acetaldehyde and methyl formate were obtained as the second and third product. Additionally, similar tendency of potential dependency suggests that these chemicals could be directly involved in butanol formation pathway. In conventional thermal process for butanol production, propylene is converted to butanal, through C-C bond formation with CO, and to butanol. Interestingly, although propylene has been detected as a product in polycrystalline Cu, it was not observed even in trace amounts in our experiments. Furthermore, mutually exclusive appearance of C_3 and C_4 chemicals also indicated that butanol is not formed from sequential chain addition to C_3 products. Recently, acetaldehyde has been highlighted as key intermediate in ethanol formation and was theoretically proposed to serve as source for C_4 products through Aldol reaction without electron involvement[49]. Thus, as a model reaction to prove role of acetaldehyde, we intentionally added acetaldehyde to the

electrolyte at concentration of 40 mM. Then the solution was stored in four different headspace vials. Each vial contained no electrode, Cu foil electrode, Ti foil electrode and $Cu_{40}Ti_{60}$ electrode in it. Aldol reaction was conducted inside vials for a long time. After overnight experiment, 0.5 μM, 0.64 μM, 0.71 μM and 0.77 μM of crotonaldehyde was detected by HS GC-MS, respectively. This is a strong evidence that amorphous CuTi electrode can also work as a catalyst for Aldol reaction without potential at room temperature. Especially, formation of 4.6 μM of crotonaldehyde at pH 10 condition indicates that Aldol reaction was accelerated by basic condition at the surface of electrode. By matching this result with detection of crotonaldehyde after bulk electrolysis confirms that Aldol reaction takes part during the reaction. Additionally, we performed bulk electrolysis at −1.3 V with 2 mM, 10 mM, 15 mM, 18 mM and 20 mM acetaldehyde solution in 0.1 M $KHCO_3$. According to UV-Vis spectra, several peaks were detected at 278 nm, 330 nm and 410 nm, which correspond to 3-hydroxybutanal and its reaction products with acetaldehyde (Figure 3.20)[50]. In biological systems, 3-hydroxybutanal is precursor to butanol[33]. Additionally, in high-performance liquid chromatography (HPLC) spectra, butanol and ethanol were detected with Faradaic efficiencies of 18.2% and 65.3%, respectively (Figure 3.21). When potential was not applied, none of the products were observed.

These clearly indicate two acetaldehyde are condensed to produce 3-hydroxybutanal, through Aldol reaction, and the 3-hydroxybutanal is subsequently reduced to crotonaldehyde than to butanol.

Another model reaction is conversion of methyl formate to acetaldehyde. The reaction was conducted in the presence of methyl formate with concentration of 2 mM, 5 mM, 10 mM, 15 mM, and 20 mM. According to ^{1}H-NMR spectra, methyl formate was converted to acetate and acetaldehyde with conversion efficiencies of 2.1% and 7.8%, respectively (Figure 3.22, Figure 3.23). Trace amount of butanol is also observed. In case of polycrystalline Cu, the yields were 1.2% for acetate and 1.3% for acetaldehyde, indicating amorphous $Cu_{40}Ti_{60}$ electrode was outperformed for methyl formate conversion. As mentioned above, it is reported that methyl formate can be transformed to acetate by reassigning methyl group or carbonyl group without electron involvement, called isomerization reaction; then the acetate is subsequently protonated to acetaldehyde[48]. Because increasing amount of carbon monoxide was observed over the course of reaction, it is expected that carbonyl group may participate in isomerization (Figure 3.24). Additionally, although the exact reaction pathway is still elusive, it is expected methyl formate is produced by condensation of formate and methanol similar to the thermal process[51]. Taken together, as

shown in Figure 3.25, we proposed reaction pathway as follows; 1) adsorption of CO_2 on electrode 2) conversion of adsorbate to methyl formate, 3) isomerization of methyl formate to acetate followed by sequential protonation to acetaldehyde and 4) Aldol reaction of acetaldehyde to produce 3-hydroxybutanol, which is further reduced to butanol.

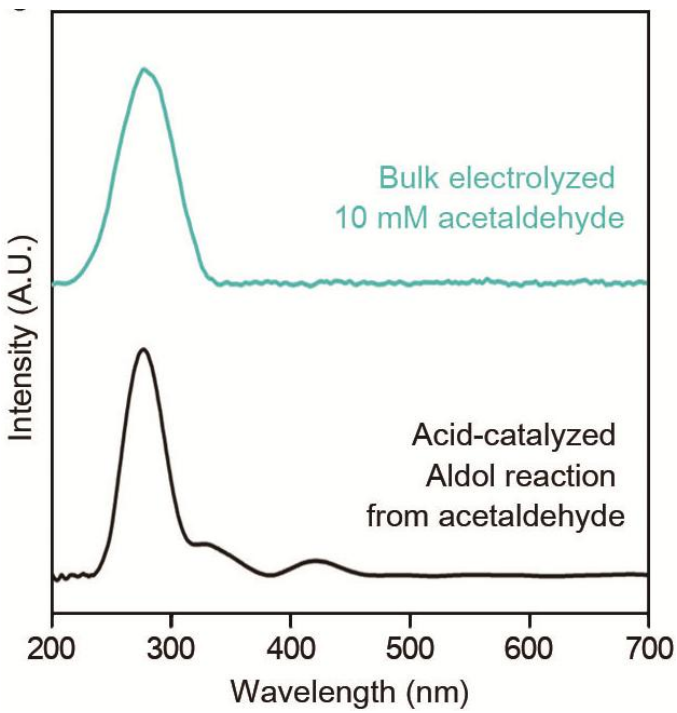

Figure 3.20 UV−Vis spectra of 10 mM of acetaldehyde (light blue) after bulk electrolysis.

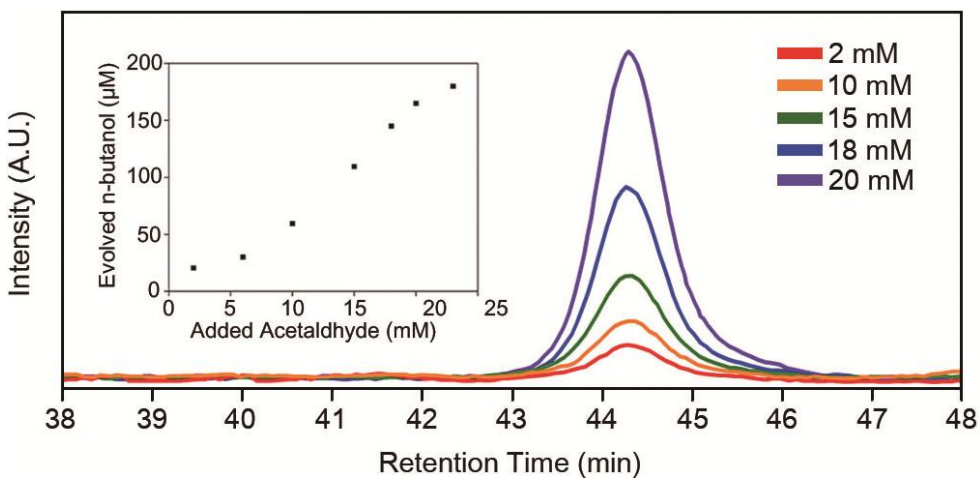

Figure 3.21 Enhanced formation of butanol by adding controlled amount of acetaldehyde in electrolyte. As added amount of acetaldehyde increased, butanol production accelerated quantitatively, as depicted in the inset.

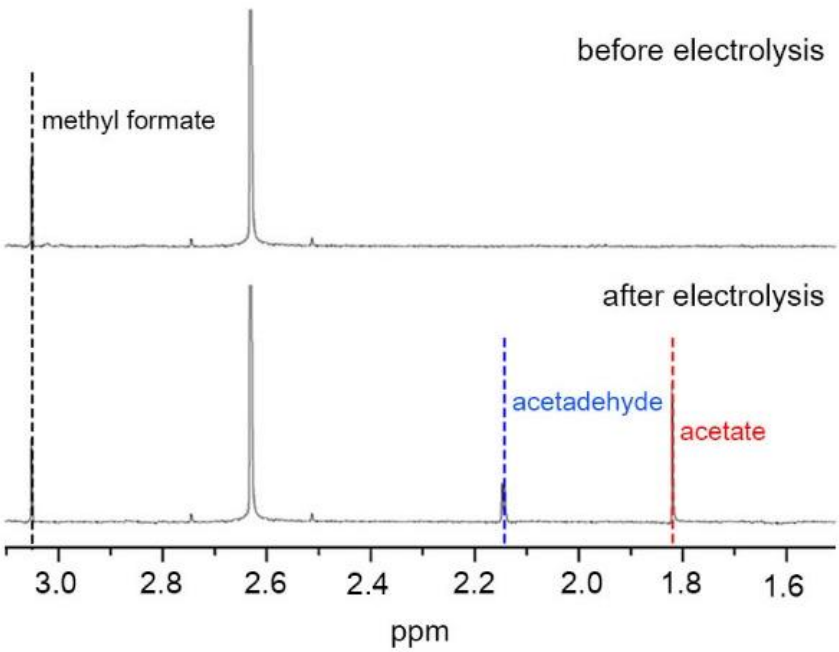

Figure 3.22 ^{1}H−NMR spectra of liquid products before and after bulk electrolysis at −1.3 V vs. NHE.

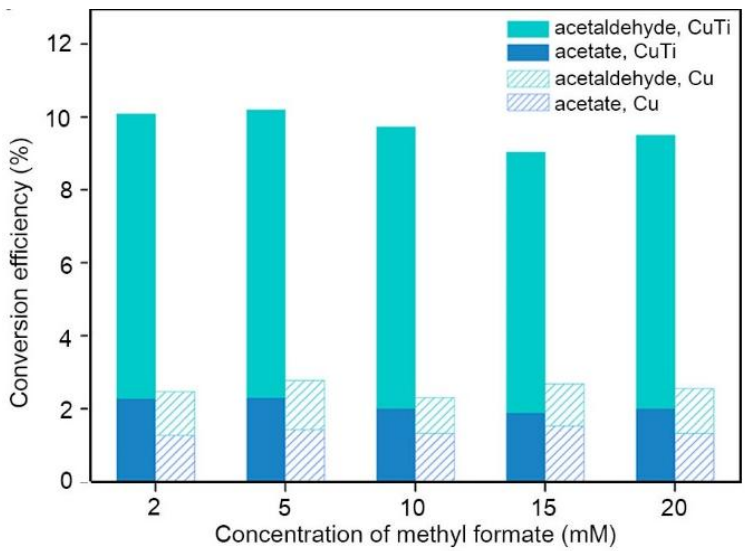

Figure 3.23 Conversion efficiency of methyl formate to acetaldehyde and acetate on amorphous CuTi and polycrystalline Cu.

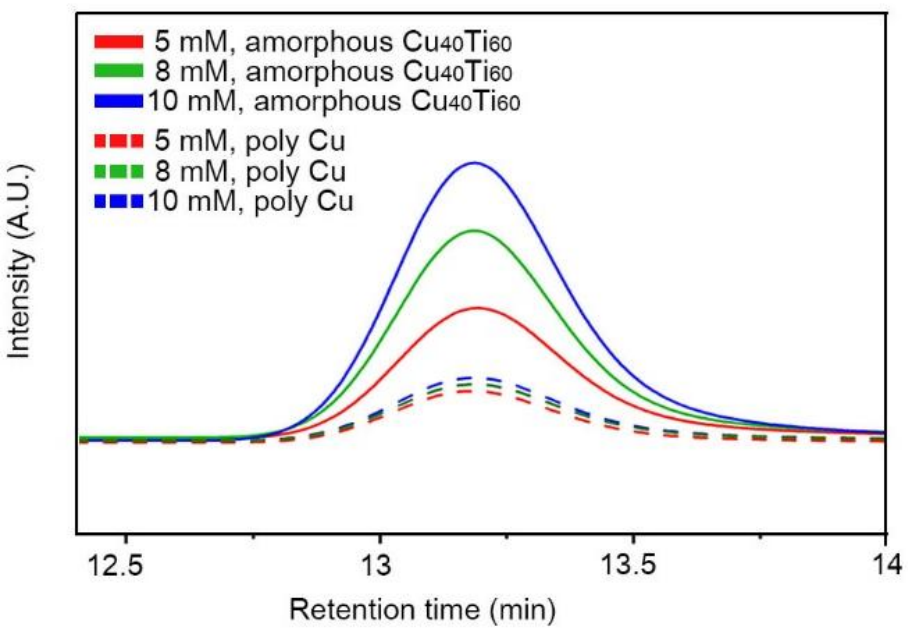

Figure 3.24 Gas chromatograms of evolved CO after the reaction with methyl formate, compared with those from polycrystalline Cu electrode under the equivalent conditions.

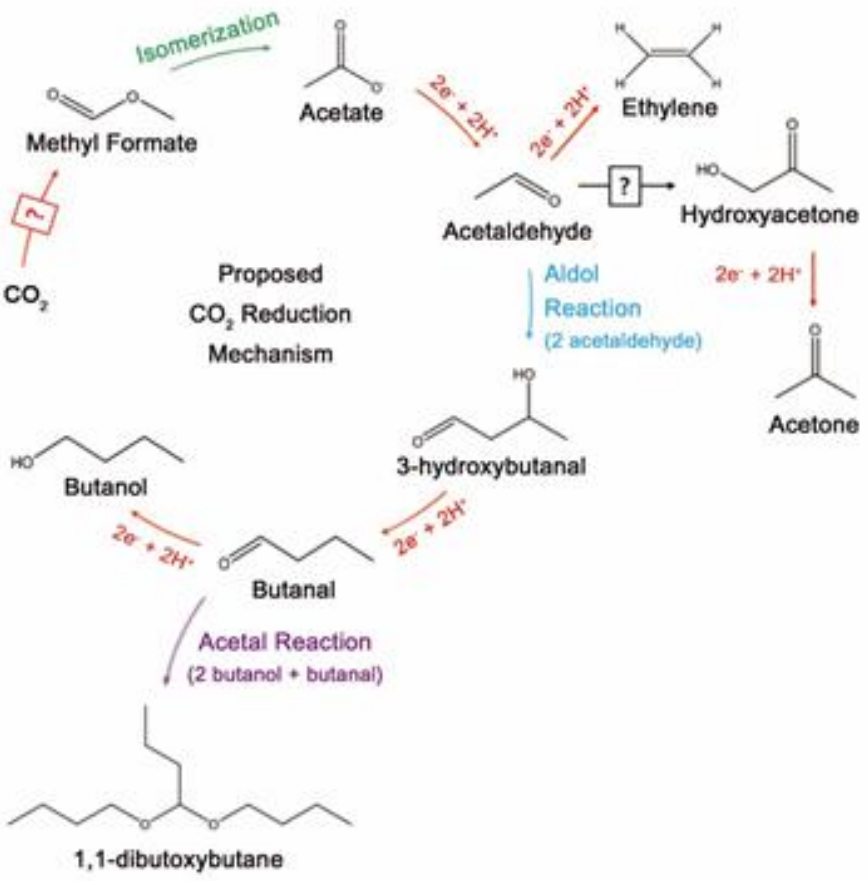

Figure 3.25 Proposed reaction mechanism of CO_2 to butanol conversion. 24 electron and proton involving reaction pathway of butanol formation. Red arrows indicate reaction steps that involve protons and electrons, whereas colored arrows indicate rearrangement of functional group (green) and condensation between the intermediates (light blue and purple).

Chapter 4. Conclusion

In conclusion, we reported amorphous Cu–Ti alloy as a new platform for electrochemical CO_2 conversion and evaluated its superior activity to form long hydrocarbon chain under modest potential range. Distorting atomic configuration of alloy, accompanied by tuning its chemical composition, resulted in high binding affinity for carbon oxygenates and facilitated C–C coupling between adsorbates. Product analysis showed butanol was formed with Faradaic efficiency of 25%, which has never been achieved by any other CO_2 reduction catalysts. In addition, some products, which were never reported before such as methyl formate and 1,1–dibutoxybutane, were also detected for the first time. According to potential dependence of products, C_2 and C_4 chemicals shared similar product trends. Mutual appearance of these products suggests a strong correlation between them. Inspired by nature, we suggested possibility of C_2 coupling reaction and set up some model reactions to propose a C_4 mechanism. Our approach exploits strategy for utilizing C_2 intermediates, which can provide more versatile and energetically efficient route for producing longer chain hydrocarbons.

References

1. Meehl, G. a, Washington, W. M. & Collins, W. D. How much more global warming and sea level rise? *Science.* **307,** 1769–1773 (2009).

2. Temperature Anomalies over Land and over Ocean. <http://data.giss.nasa.gov/>

3. Collins, M. *et al.* in *Climate change 2013: the physical science basis. Contribution of Working Group I to the Fifth Assessment Report of the Intergovernmental Panel on Climate Change* 1029–1136 (Cambridge University Press, 2013).

4. Atmospheric CO_2 at Mauna Loa Observatory. at <https://www.esrl.noaa.gov/>

5.O'Neill, B. C. *et al.* IPCC reasons for concern regarding climate change risks. *Nat. Clim. Chang.* **7,** 28–37 (2017).

6. Lim, X. How to make the most of carbon dioxide. *Nature* **526,** 628 (2015).

7. Gielen, D., Boshell, F. & Saygin, D. Climate and energy challenges for materials science. *Nat. Mater.* **15,** 117–120 (2016).

8. Kuhl, K. P., Cave, E. R., Abram, D. N. & Jaramillo, T. F. New insights into the electrochemical reduction of carbon dioxide on metallic copper surfaces. *Energy Environ. Sci.* **5,** 7050 (2012).

9. Carbon capture and storage – full chain. at <http://www.sccs.org.uk/>

10. Qiao, J., Liu, Y., Hong, F. & Zhang, J. A review of catalysts for the electroreduction of carbon dioxide to produce low-carbon fuels. *Chem. Soc. Rev.* **43,** 631–675 (2014).

11. Hori, Y. in *Modern Aspects of Electrochemistry* 89–189 (Springer New York, 2008).

12. Zhang, S., Kang, P. & Meyer, T. J. Nanostructured Tin Catalysts for Selective Electrochemical Reduction of Carbon Dioxide to Formate. *J. Am. Chem. Soc.* **136,** 1734–1737 (2014).

13. Kumar, B. *et al.* Renewable and metal-free carbon nanofibre catalysts for carbon dioxide reduction. *Nat. Commun.* **4,** 2819 (2013).

14. Lin, S. *et al.* Covalent organic frameworks comprising cobalt porphyrins for catalytic CO_2 reduction in water. *Science (80-.).* **349,** 1208–1213 (2015).

15. Barton, E. E., Rampulla, D. M. & Bocarsly, A. B. Selective Solar-Driven Reduction of CO_2 to Methanol Using a Catalyzed p-GaP Based Photoelectrochemical Cell. *J. Am. Chem. Soc.* **130,** 6342–6344 (2008).

16. Saveant, J. & Tard, C. Attempts To Catalyze the Electrochemical CO_2 -to-Methanol Conversion by Biomimetic $2e^- + 2H^+$ Transferring Molecules. *J. Am. Chem. Soc.* **138,** 1017–1021 (2016).

17. DeWulf, D. W. Electrochemical and Surface Studies of Carbon Dioxide Reduction to Methane and Ethylene at Copper Electrodes in Aqueous Solutions. *J. Electrochem. Soc.* **136,** 1686 (1989).

18. Roberts, F. S., Kuhl, K. P. & Nilsson, A. High Selectivity for Ethylene from Carbon Dioxide Reduction over Copper Nanocube Electrocatalysts. *Angew. Chemie* **127,** 5268–5271 (2015).

19. Lee, S., Kim, D. & Lee, J. Electrocatalytic Production of C_3-C_4 Compounds by Conversion of CO_2 on a Chloride-Induced Bi-Phasic Cu_2O-Cu Catalyst. *Angew. Chemie* **54,** 1–6 (2015).

20. Peterson, A. A. & Nørskov, J. K. Activity Descriptors for CO_2 Electroreduction

to Methane on Transition-Metal Catalysts. *J. Phys. Chem. Lett.* **3,** 251–258 (2012).

21. Hori, Y., Takahashi, I., Koga, O. & Hoshi, N. Electrochemical reduction of carbon dioxide at various series of copper single crystal electrodes. *J. Mol. Catal. A Chem.* **199,** 39–47 (2003).

22. Zhu, W. *et al.* Active and selective conversion of CO_2 to CO on ultrathin Au nanowires. *J. Am. Chem. Soc.* **136,** 16132–16135 (2014).

23. Verdaguer-casadevall, A. *et al.* Probing the Active Surface Sites for CO Reduction on Oxide-Derived. *J. Am. Chem. Soc.* **137,** 9808–9811 (2015).

24. Gao, S. *et al.* Partially oxidized atomic cobalt layers for carbon dioxide electroreduction to liquid fuel. *Nature* **529,** 68–71 (2016).

25. Gattrell, M., Gupta, N. & Co,. A review of the aqueous electrochemical reduction of CO_2 to hydrocarbons at copper. *J. Electroanal. Chem.* **594,** 1–19 (2006).

26. Luo, W., Nie, X., Janik, M. J. & Asthagiri, A. Facet Dependence of CO_2 Reduction Paths on Cu Electrodes. *ACS Catal.* **6,** 219–229 (2016).

27. Le, M. *et al.* Electrochemical Reduction of CO_2 to CH_3OH at Copper Oxide Surfaces. *J. Electrochem. Soc.* **158,** E45–E49 (2011).

28. Roberts, F. S., Kuhl, K. P. & Nilsson, A. High selectivity for ethylene from carbon dioxide reduction over copper nanocube electrocatalysts. *Angew. Chemie - Int. Ed.* **54,** 5179–5182 (2015).

29. Tao, L. *et al.* Techno-economic analysis and life-cycle assessment of cellulosic isobutanol and comparison with cellulosic ethanol and n-butanol. *Biofuels, Bioprod. Biorefining* **8,** 30–48 (2014).

30. Lan, E. I. & Liao, J. C. ATP drives direct photosynthetic production of 1-butanol in cyanobacteria. *Proc. Natl. Acad. Sci. U. S. A.* **109,** 6018–23 (2012).

31. Li, H. *et al.* Integrated Electromicrobial Conversion of CO_2 to Higher Alcohols. *Science (80-.).* **335,** 1596–1596 (2012).

32. Lan, E. I. & Liao, J. C. Metabolic engineering of cyanobacteria for 1-butanol production from carbon dioxide. *Metab. Eng.* **13,** 353–363 (2011).

33. Bond-Watts, B. B., Bellerose, R. J. & Chang, M. C. Y. Enzyme mechanism as a kinetic control element for designing synthetic biofuel pathways. *Nat. Chem. Biol.* **7,** 222–227 (2011).

34. Parkin, A., Seravalli, J., Vincent, K. A., Ragsdale, S. W. & Armstrong, F. a. Rapid and efficient electrocatalytic CO_2/CO interconversions by Carboxydothermus hydrogenoformans CO dehydrogenase I on an electrode. *J. Am. Chem. Soc.* **129,** 10328–10329 (2007).

35. Halmann, M. M. *Chemical fixation of carbon dioxide- Methods for recycling CO_2 into useful products*. (CRC Press, 1993).

36. Dean, J. A. *Lange's Handbook of chemistry*. (McGraw-Hill, INC., 1999).

37. Idriss, H., Kim, K. S. & Barteau, M. A. Carbon-Carbon Bond Formation via Aldolization of Acetaldehyde on Single Crystal and Polycrystalline TiO_2 Surfaces. *Journal of Catalysis* **139,** 119–133 (1993).

38. Hansen, H. A., Shi, C., Lausche, A., Peterson, A. & Nørskov, J. K. Bifunctional alloys for the electroreduction of CO_2 and CO. *Phys. Chem. Chem. Phys.* 9194–9201 (2016).

39. Lim, H. K. *et al.* Embedding covalency into metal catalysts for efficient

electrochemical conversion of CO_2. *J. Am. Chem. Soc.* **136,** 11355–11361 (2014).

40. Dunnington, B. D. & Schmidt, J. R. Molecular bonding-based descriptors for surface adsorption and reactivity. *J. Catal.* **324,** 50–58 (2015).

41. Johnson, W. L. Bulk Glass-Forming Metallic Alloys: Science and Technology. *MRS Bull.* **24,** 42–56 (1999).

42. Zhang, S., Fan, G. & Li, F. Lewis-base-promoted copper-based catalyst for highly efficient hydrogenation of dimethyl 1,4-cyclohexane dicarboxylate. *Green Chem.* **15,** 2389 (2013).

43. Yu, S., Wang, X. & Huang, W. Preparation and characterization of nonmetal promoter modified CuZnAl catalysts for higher alcohol from synthesis gas through complete liquid phase. *Turk. J. Chem.* 381–387 (2014). doi:10.3906/kim-1212-67

44. Xiong, L.-B., Li, J.-L., Yang, B. & Yu, Y. Ti^{3+} in the Surface of Titanium Dioxide: Generation, Properties and Photocatalytic Application. *J. Nanomater.* **2012,** 1–13 (2012).

45. Brown, W. H., Foote, C. S. Iverson, B. L., Anslyn, E. *Organic Chemistry*. *Business* (Brooks/Cole Cengage Learning, 2009).

46. Hori, Y., Murata, A. & Takahashi, R. Formation of Hydrocarbons in the Electrochemical Reduction of Carbon Dioxide at a Copper Electrode in Aqueous Solution. *J. Chem. Soc., Faraday Trans. 1* **85,** 2309–2326 (1989).

47. Hallmann, C., van Aarssen, B. G. K. & Grice, K. Relative efficiency of free fatty acid butyl esterification. *J. Chromatogr. A* **1198–1199,** 14–20 (2008).

48. Ohnishi, T., Suzuki, T., Yamakawa, T. & Shinoda, S. Isomerization of methyl formate to acetic acid catalysed by the Ru(II)-Sn(II) heteronuclear cluster

complex $[Ru(SnCl_3)_5(PPh_3)]^{3-}$. *J. Mol. Catal.* **84,** 51–58 (1993).

49. Bertheussen, E. *et al.* Acetaldehyde as an Intermediate in the Electroreduction of Carbon Monoxide to Ethanol on Oxide–Derived Copper. *Angew. Chemie – Int. Ed.* **94305,** 1472–1476 (2015).

50. Casale, M. *et al.* Kinetics of acid–catalyzed aldol condensation reactions of aliphatic aldehydes. *Atmos. Environ.* **41,** 6212–6224 (2007).

51. Sexton, B. A., Hughes, A. E. & Avery, N. R. Surface intermediates in the reaction of methanol, formaldehyde and methyl formate on copper (110). *Appl. Surf. Sci.* **22–23,** 404–414 (1985).

국 문 초 록

이산화탄소를 전기환원하여 유용한 연료를 생산하는 방법은 재생 에너지를 활용할 수 있고, 물을 양성자 원료로 사용한다는 점에서 다른 이산화탄소를 화학 공급 원료로 전환하는 방법에 비해 큰 장점을 가지고 있다. 현재까지 이산화탄소를 포름산, 일산화탄소, 메탄올 등의 유용한 연료로 전기환원한 사례들이 보고되었지만 C_4 혹은 그보다 긴 탄소화합물을 주생성물로 보고한 사례는 없다. 그러므로 우리는 현재까지 효율적으로 긴 탄소화합물을 생산할 수 있는 새로운 촉매 플랫폼 개발에 초점을 맞추고 연구하였다.

본 연구에서 우리는 비정질 Cu-Ti 합금을 이산화탄소를 긴 탄소화합물로 환원시키기 위한 전극으로 사용하였다. 순환전압 전류법으로 세 전극($Cu_{40}Ti_{60}$, $Cu_{50}Ti_{50}$, $Cu_{60}Ti_{40}$)의 이산화탄소 전기환원 특성을 확인해 본 결과, 비정질 $Cu_{40}Ti_{60}$ 전극이 가장 우수한 촉매 특성을 가지고 있으며, 가장 적은 과전압이 필요하다는 사실을 확인하였다. CO_2-TPD를 통해서 확인해본 결과, 이 전극의 우수한 특성이 전극 표면에서 반응 중간체인 탄소 산화물들과의 결합이 강하게 이루어지기 때문이었다. 이러한 결과는 Ti 원자가 반응 중간체들과 전극 표면 사이의 결합을 강하게 해준다는 것을 의미한다.

그 다음으로 우리는 비정질 $Cu_{40}Ti_{60}$ 전극이 이산화탄소를 부탄올로 환원시킬 수 있다는 사실을 밝혔다. 기체 크로마토그래피, 핵자기공명분광

법 등을 활용해 생성물을 분석한 결과, 부탄올 및 아세트알데하이드, 메틸 포르메이트, 일산화탄소, 수소 등이 생성되었다. 이를 바탕으로 우리는 전기화학 반응을 통해 이산화탄소를 최초로 C_4 화합물(부탄올, 효율 : 25%)로 환원하였다고 보고하였다. 이 결과는 비정질 특성이 탄소 산화물들이 전극 표면에 강하게 붙어있을 수 있도록 유도하며, 탄소 간의 결합 형성에 유리한 조건임을 의미한다. 추가로 반응 메커니즘에 대한 정보를 얻기 위하여 서로 다른 포텐셜에서 실험을 하고 생성물이 어떻게 바뀌는지 확인하였다. 그 결과 부탄올 생성 과정은 C_3 중간체를 거치지 않으며 두 개의 C_2 반응 중간체들 간의 반응을 거친다.

본 연구를 통해서 우리는 비정질 $Cu_{40}Ti_{60}$ 전극을 활용하여 이산화탄소를 부탄올로 전기환원 시키는데 성공하였다. 이러한 연구 결과는 이산화탄소를 고부가가치 혹은 긴 탄소화합물로 전환시키는 반응 경로에 대한 새로운 안목을 제시하였으며, 그 경로에 있어서 C_2 중간체들 간의 반응이 중요하다는 사실을 제공하였다. 또한, 비정질 합금을 활용하였기 때문에 원자 조성과 배열을 제어할 수 있었다는 점에서 큰 의의를 갖는다.